An enriched finite element model with q-refinement for radiative boundary layers in glass cooling

An enriched finite element model with q-refinement for radiative boundary layers in glass cooling

M. Shadi Mohamed[*], Mohammed Seaid[†], Jon Trevelyan[†], Omar Laghrouche[*]

Abstract

Radiative cooling in glass manufacturing is simulated using the partition of unity finite element method. The governing equations consist of a semi-linear transient heat equation for the temperature field and a stationary simplified P_1 approximation for the radiation in non-grey semitransparent media. To integrate the coupled equations in time we consider a linearly implicit scheme in the finite element framework. A class of hyperbolic enrichment functions is proposed to resolve boundary layers near the enclosure walls. Using an industrial electromagnetic spectrum, the proposed method shows an immense reduction in the number of degrees of freedom required to achieve a certain accuracy compared to the conventional h-version finite element method. Furthermore the method shows a stable behaviour in treating the boundary layers which is shown by studying the solution close to the domain boundaries. The time integration choice is essential to implement a q-refinement procedure introduced in the current study. The enrichment is refined with respect to the steepness of the solution gradient near the domain boundary in the first few time steps and is shown to lead to a further significant reduction on top of what is already achieved with the enrichment. The performance of the proposed method is analyzed for glass annealing in two enclosures where the simplified P_1 approximation solution with the partition of unity method, the conventional finite element method and the finite difference method are compared to each other and to the full radiative heat transfer as well as the canonical Rosseland model.

Keywords. Finite element method; Partition of unity method; Radiative heat transfer; Simplified P_1 approximation; Glass cooling; Boundary layers

1 Introduction

Heat transfer phenomena involve different mechanisms such as thermal conduction, convection and radiation. The first two mechanisms are the most commonly considered in heat transfer simulations while the thermal radiation is often neglected because of (i) the high computational cost, and (ii) the uncertainty related to the optical properties of the materials being modelled, see for example [23, 25] and further references are cited therein. Another complexity is related to the complicated physical models which need to be solved in order to consider thermal radiation [5]. The computational cost involved in considering thermal radiation is mainly caused by the wide spectrum of electromagnetic waves that are emitted from a thermally radiating material [3]. The optical properties of a material define active frequency bands through which most of the heat energy radiates. The model describing the thermal radiation needs to be solved for each of these frequency bands in order to estimate the cumulative heat energy emitted through radiation. The change in transfer of the heat energy through different mechanisms results in a change in the material temperature [24]. Hence, the obtained radiative temperature needs to be accounted for when considering these mechanisms in the time domain, where the thermal radiation adds an extra complexity. The radiation waves move at the speed of light whereas other mechanisms happen at much slower time scales. Thus the radiation scale has an effect on the scale used in the solution of other coupled mechanisms, see for instance [11, 13].

[*]Institute for Infrastructure and Environment, Heriot-Watt University, Edinburgh EH14 4AS, UK
[†]School of Engineering and Computing Sciences, University of Durham, South Road, Durham DH1 3LE, UK

Although it may be possible in some cases to neglect it, Radiative Heat Transfer (RHT) has important applications in engineering and science: nuclear power plants [12], turbojet engines [15] and thermal management in space [7] are only a few examples where ignoring the RHT can introduce significant computational errors [16]. In the full simulation of RHT systems, the radiative transfer, which is an integro-differential equation, must be solved along with the partial differential equations of material, momentum, energy transport and chemical reactions as a fully coupled system [15]. The most accurate procedures available in the literature for computing radiative transfer are the zonal and Monte Carlo methods [16]. However, these methods are not widely applied in comprehensive heat transfer calculations due to their large computational time and storage requirements. Also, the equations of radiative transfer are presented in a non-differential form, which presents a significant inconvenience when they are solved in conjunction with the differential equations of heat conduction, flow and combustion. Most of the current work on modelling energy transport in high-temperature media or chemically reacting flows uses Computational Fluid Dynamics (CFD) codes; see for instance [21, 15, 26]. Therefore, the models for solving the radiative transfer must be compatible with the numerical methods employed to solve the reacting flow equations. The zonal and Monte Carlo methods for solving radiative transfer problems are incompatible with the mathematical formulations used in CFD codes. The S_n discrete-ordinate methods [2] appear to be reasonable compromises for solving the radiative transfer equations, but still one has to deal with large systems of algebraic equations, resulting from discretizing angular and spatial coordinates in each frequency band, that may be detrimental to the efficiency of the CFD code. For more details, the interested reader is referred to [25, 24].

In the field of glass manufacturing, the quality of the final product strongly depends on controlling the annealing process as molten glass is cooled down to the room temperature. Recent developments in optical industries such as display technologies and lens manufacturing require glass objects having specific optical and physical properties. This has led to an increasing interest in accurate mathematical models which can predict the heat transfer involved in glass manufacturing, and hence to a better control over the annealing process. Among these models, the Rosseland approximation [22] could be the most efficient, but fails to resolve accurately the thermal boundary layers in the cooling processes mainly because it does not address the RHT. The simplified $\mathrm{P_N}$ approximations of RHT equations have been widely used in the literature. These approximations were first proposed in [4] and theoretically studied in [9]. In [3] the simplified $\mathrm{P_N}$ approximations were implemented for radiation in gas turbines, while in [10, 27] they were studied for the RHT in glass manufacturing. These simplified models are derived using an asymptotic analysis and they perform very well when the medium under consideration is isotropic and optically thick (opaque). In fact, in an opaque medium the system is close to a radiative equilibrium for which the assumptions of the simplified $\mathrm{P_N}$ equations are satisfied. A major advantage in the simplified $\mathrm{P_N}$ approximations consists in the fact that the RHT equations are transformed to a mixed set of parabolic and elliptic equations independent of the angular directions, facilitating their numerical solution. Furthermore, comparisons presented in the previous references proved that in optically thick media (large absorption) the simplified $\mathrm{P_N}$ models approach the full RHT problem with a lower computational cost and with greater accuracy than those obtained by the classical Rosseland approach traditionally used in many applications in glass manufacturing. In this paper, we adopt the simplified $\mathrm{P_1}$ approximation to the RHT problem. We consider glass cooling models with eight frequency bands kindly provided by ITWM [6] and also analyzed in [10, 8] among others.

A key feature of the RHT in glass manufacturing is the existence of very high thermal gradients at the domain boundary at the start of the cooling process. One approach to capturing these steep gradients with numerical methods such as the conventional Finite Element Method (FEM) is to use a highly refined mesh close to the boundaries [8]. However, the required refinement level, coupled with small time steps needed to capture the thermal radiation, may cause an extended solution time which can become prohibitive for industrial purposes. A more sophisticated approach arises from application of different variations of the partition of unity technique [14]; this involves enrichment of the finite element approximation space in order to become more efficient in dealing with high gradients. A relatively early work dealing with the enriched FEM for diffusion and convection problems can be found in [19] where the authors enriched the FEM with the analytical solution of the considered problem in one space dimension. Further enrichment approaches have since been applied to transient thermal effects. In [28] an enrichment approach was developed to deal

with time-dependent geothermal problems. The transient nature of the solution was accounted for through optimizing the enrichment at each time step. In a later development a global-local enriched formulation for transient heat transfer, in which a linear interpolation basis is augmented by an exponential function of space or space and time, was presented in [20]. Time-dependent shape functions are used to handle the transient nature of the problem and these are supplemented by local analysis using various techniques in regions of high thermal gradients. Another enrichment strategy was developed in [17] where, instead of time-dependent enrichment, the transient nature of the problem is expressed in terms of Gaussian function combinations that mimic the time evolution of the solution as well as its spatial variation. The main advantage of such a strategy is allowing the linear system built at the first time step to be retained for each subsequent time step with only updating the right hand side. The approach has recently been successfully applied to conduction-radiation in diffusive grey media [18] where a combination of hyperbolic and Gaussian functions were used to recover the solution. In the current study this approach is further developed to solve the frequency-dependent RHT in glass cooling problems. In our previous work [18], the radiation is assumed to be active at a single frequency which is rarely used to simulate conduction-radiation in semitransparent materials. However, in the general case such as in glass, the thermal radiation can be active at a wide spectrum of frequencies, see [5, 10] among others. The considered simplified P_1 approximation requires decomposing the continuous spectrum into several frequency bands, and hence the thermal radiation must be evaluated at each band. To address this issue a refinement approach is proposed for the enrichment in order to reduce the computational cost particularly when a high number of frequency bands is needed for a given optical spectrum. Special attention is paid to numerical solutions within the boundary layers and at early time steps which are particularly important in the control of the glass annealing process. The performance of the proposed method is compared to the h-version FEM and the Finite Difference Method (FDM) with a further verification using the full radiative transfer solution.

This paper is organized as follows. The governing equations for the frequency-dependent RHT in glass cooling are stated in section 2. In section 3, we state the time discretization approach of a linearly implicit scheme for the time integration while the variational formulation for the space discretization is established in section 4. The approximation by enriched finite elements for the numerical solution of the coupled heat transfer equations is then discussed in section 5. Finally the numerical results for two test examples in glass cooling are presented in section 6. Section 7 contains concluding remarks.

2 Equations for radiative heat transfer in glass cooling

Let Ω be a geometrical domain, with boundary $\partial\Omega$, of an absorbing and emitting glass material. We seek the temperature distribution $T(\mathbf{x},t)$, where $\mathbf{x}\in\Omega$ and t is time, with a given initial distribution

$$T(\mathbf{x},0)=T_0(\mathbf{x}),\qquad \mathbf{x}\in\Omega. \tag{2.1}$$

The heat conduction in the medium Ω is described by the energy equation

$$\rho_g c_g\frac{\partial T}{\partial t}-\nabla\cdot(k_c\nabla T)=-\int_{\nu_0}^{\infty}\int_{\mathbb{S}^2}\kappa(\nu)\Big(B(T,\nu,n_{\mathrm{g}})-I\Big)d\mathbf{s}d\nu,\quad (\mathbf{x},t)\in\Omega\times[0,t_{end}), \tag{2.2}$$

where ρ_g denotes the glass density, c_g the specific heat capacity of the glass, ν the frequency, k_c the thermal conductivity and κ the absorption coefficient. On the boundary, the heat flux $k_c\mathbf{n}(\hat{\mathbf{x}})\cdot\nabla T$ is defined by heat convection and diffuse surface radiation

$$k_c\mathbf{n}(\hat{\mathbf{x}})\cdot\nabla T+h_c(T-T_b)=\alpha\pi\int_0^{\nu_0}\Big(B(T_b,\nu,n_{\mathrm{b}})-B(T,\nu,n_{\mathrm{b}})\Big)d\nu,\quad (\hat{\mathbf{x}},t)\in\partial\Omega\times[0,t_{end}), \tag{2.3}$$

where h_c is the convective heat transfer coefficient, T_b is a given ambient temperature of the surrounding, $\mathbf{n}(\hat{\mathbf{x}})$ denotes the outward normal at $\hat{\mathbf{x}}$ with respect to $\partial\Omega$, α is the mean hemispheric surface emissivity in the opaque spectral region $\nu\in[0,\nu_0]$, where radiation is completely absorbed, n_{b} and n_{g} are the refractive indices of the surrounding medium and the glass material, respectively. In the above equations, $B(T,\nu,n)$ is

the spectral intensity of the black-body radiation defined by the Planck function in a medium with refractive index n. It is given by

$$B(T,\nu,n)=\frac{2h_P\nu^3}{c_0^2}n^2\big(\exp(h_P\nu/\kappa_BT)-1\big)^{-1}, \tag{2.4}$$

where h_P, κ_B and c_0 are Planck's constant, Boltzmann's constant and the speed of radiation propagation in the vacuum, respectively [15]. The spectral intensity $I=I(\mathbf{x},\mathbf{s},\nu)$ at the point $\mathbf{x}$, at the frequency ν and along the direction $\mathbf{s}$, is obtained from the radiative transfer equation

$$\forall\nu>\nu_0:\quad \mathbf{s}\cdot\nabla I+\kappa(\nu)I=\kappa(\nu)B(T,\nu,n_{\rm g}),\quad (\mathbf{x},\mathbf{s})\in\Omega\times\mathbb{S}^2, \tag{2.5}$$

where $\mathbb{S}^2$ denotes the unit sphere. At the boundary we consider the transmitting and specular reflecting condition

$$I(\hat{\mathbf{x}},\mathbf{s},\nu)=\varrho(\mathbf{n}\cdot\mathbf{s})I(\hat{\mathbf{x}},\mathbf{s}',\nu)+\big(1-\varrho(\mathbf{n}\cdot\mathbf{s})\big)B(T_b,\nu,n_{\rm g}),\quad (\hat{\mathbf{x}},\mathbf{s})\in\partial\Omega^-\times\mathbb{S}^2, \tag{2.6}$$

where the boundary region $\partial\Omega^-$ is defined as

$$\partial\Omega^-=\Big\{\hat{\mathbf{x}}\in\partial\Omega:\quad \mathbf{n}(\hat{\mathbf{x}})\cdot\mathbf{s}<0\Big\},$$

and $\mathbf{s}'$ is the specular reflection of $\mathbf{s}$ on $\partial\Omega$ given by

$$\mathbf{s}'=\mathbf{s}-2(\mathbf{n}\cdot\mathbf{s})\mathbf{n}.$$

In (2.6), $\varrho\in[0,1]$ is the reflectivity obtained according to the Fresnel and Snell laws. Thus, for an incident angle $\theta_{\rm g}$ given by $\cos\theta_{\rm g}=|\mathbf{n}\cdot\mathbf{s}|$ and the Snell law

$$n_{\rm b}\sin\theta_{\rm b}=n_{\rm g}\sin\theta_{\rm g},$$

the reflectivity $\varrho(\mu)$, $\mu=|\mathbf{n}\cdot\mathbf{s}|$, is defined by the Fresnel law

$$\varrho(\mu)=\begin{cases}\dfrac{1}{2}\left(\dfrac{\tan^2(\theta_{\rm g}-\theta_{\rm b})}{\tan^2(\theta_{\rm g}+\theta_{\rm b})}+\dfrac{\sin^2(\theta_{\rm g}-\theta_{\rm b})}{\sin^2(\theta_{\rm g}+\theta_{\rm b})}\right), & \text{if}\quad |\sin\theta_{\rm g}|\le\dfrac{n_{\rm b}}{n_{\rm g}},\\[2ex] 1, & \text{otherwise.}\end{cases}$$

We assume that $n_{\rm g}>n_{\rm b}$ and the hemispheric emissivity α is related to the reflectivity ϱ by

$$\alpha=2n_{\rm g}\int_0^1\Big(1-\varrho(\mu)\Big)d\mu.$$

The RHT equations (2.1)-(2.6) can be reformulated in a dimensionless form as

$$\begin{aligned}
\varepsilon^2\frac{\partial T}{\partial t}-\varepsilon^2\nabla\cdot\big(k_c\nabla T\big) &= -\int_{\nu_0}^{\infty}\kappa(\nu)\left(4\pi B(T,\nu,n_{\rm g})-\int_{\mathbb{S}^2}I(\mathbf{x},\mathbf{s},\nu)d\mathbf{s}\right)d\nu,\\
\forall\,\nu>\nu_0:\qquad \varepsilon\mathbf{s}\cdot\nabla I+\kappa(\nu)I &= \kappa(\nu)B(T,\nu,n_{\rm g}),\\
\varepsilon k_c\mathbf{n}(\hat{\mathbf{x}})\cdot\nabla T+h_c(T-T_b) &= \alpha\pi\int_0^{\nu_0}\Big(B(T_b,\nu,n_{\rm b})-B(T,\nu,n_{\rm b})\Big)d\nu,\\
I(\hat{\mathbf{x}},\mathbf{s},\nu) &= \varrho(\mathbf{n}\cdot\mathbf{s})I(\hat{\mathbf{x}},\mathbf{s}',\nu)+\big(1-\varrho(\mathbf{n}\cdot\mathbf{s})\big)B(T_b,\nu,n_{\rm g}),\\
T(\mathbf{x},0) &= T_0(\mathbf{x}),
\end{aligned} \tag{2.7}$$

where $\varepsilon\in(0,1]$ is a diffusion scale. Details on the passage from dimensional equations to the dimensionless system can be found in [10, 8] and are omitted here. In the present study, we assume that the spectral absorption coefficients $\kappa(\nu)$ are piecewise constants with respect to the frequency ν, *i.e.*,

$$\kappa(\nu)=\kappa_k,\qquad \forall\,\nu\in[\nu_{k-1},\nu_k),\quad k=1,2,\ldots,N, \tag{2.8}$$

with $\nu_0 = 0$, κ_k is constant and N is the total number of spectral bands. If we introduce the intensity of the kth spectral band

$$I^{(k)}(\mathbf{x}, \mathbf{s}) = \int_{\nu_{k-1}}^{\nu_k} I(\mathbf{x}, \mathbf{s}, \nu) d\nu,$$

then the RHT equations (2.7) transform to

$$\begin{aligned}
\varepsilon^2 \frac{\partial T}{\partial t} - \varepsilon^2 \nabla \cdot \big(k_c \nabla T\big) &= -\sum_{k=1}^{N} \kappa_k \Big(4\pi B^{(k)}(T, n_{\mathrm{g}}) - \varphi^{(k)}\Big), \\
\varepsilon \mathbf{s} \cdot \nabla I^{(k)} + \kappa_k I^{(k)} &= \kappa_k B^{(k)}(T, n_{\mathrm{g}}), \\
\varepsilon k_c \mathbf{n}(\hat{\mathbf{x}}) \cdot \nabla T + h_c (T - T_b) &= \alpha\pi \Big(B^{(0)}(T_b, n_{\mathrm{b}}) - B^{(0)}(T, n_{\mathrm{b}})\Big), \\
I^{(k)}(\hat{\mathbf{x}}, \mathbf{s}) &= \varrho(\mathbf{n} \cdot \mathbf{s}) I^{(k)}(\hat{\mathbf{x}}, \mathbf{s}') + \big(1 - \varrho(\mathbf{n} \cdot \mathbf{s})\big) B^{(k)}(T_b, n_{\mathrm{g}}), \\
T(\mathbf{x}, 0) &= T_0(\mathbf{x}),
\end{aligned} \tag{2.9}$$

where the mean intensity $\varphi^{(k)}$ and the Planck function $B^{(k)}$ are defined by

$$\varphi^{(k)}(\mathbf{x}) = \int_{\mathbb{S}^2} I^{(k)}(\mathbf{x}, \mathbf{s}) d\mathbf{s}, \qquad \text{and} \qquad B^{(k)}(T, n) = \int_{\nu_{k-1}}^{\nu_k} B(T, \nu, n) d\nu.$$

The RHT equations (2.7) are widely accepted as an accurate model for radiation transport in both participating and non-participating media. These equations do not have analytical solutions for arbitrary geometries and their numerical solution leads to computationally demanding problems due to the large set of dependent variables. For these reasons, numerous investigations are currently being carried out to derive approximate methods that are computationally less demanding than solving the equations (2.7). Among typical approximations to RHT we cite the Rosseland approach [22] and simplified $\mathrm{P_N}$ approximations [10, 8]. Indeed, a major reduction of the discrete phase space can be achieved if one replaces the RHT equations by a new model which only involves physical quantities independent of the angular direction. One possibility to do so is to use the so-called Simplified $\mathrm{P_N}$ ($\mathrm{SP_N}$) approximations. In this section we only set up the simplified $\mathrm{P_1}$ ($\mathrm{SP_1}$) approximation, for further details on the derivation of $\mathrm{SP_N}$ models we refer to [10]. Thus, the $\mathrm{SP_1}$ approximation for the RHT equations reads

$$\begin{aligned}
\frac{\partial T}{\partial t} - \nabla \cdot \big(k_c \nabla T\big) &= \sum_{k=1}^{N} \nabla \cdot \Big(\frac{1}{3\kappa_k} \nabla \varphi^{(k)}\Big), \\
-\nabla \cdot \Big(\frac{\varepsilon^2}{3\kappa_k} \nabla \varphi^{(k)}\Big) + \kappa_k \varphi^{(k)} &= 4\pi \kappa_k B^{(k)}(T, n_{\mathrm{g}}), \qquad k = 1, \ldots, N.
\end{aligned} \tag{2.10}$$

The boundary conditions are derived based on the asymptotic analysis in [10]. For the considered $\mathrm{SP_1}$ approximation (2.10), $\varphi^{(k)}$ satisfies the following Robin-type boundary condition

$$\varphi^{(k)} + \left(\frac{1 + 3r_2}{1 - 2r_1} \frac{2\varepsilon}{3\kappa_k}\right) \mathbf{n}(\hat{\mathbf{x}}) \cdot \nabla \varphi^{(k)} = 4\pi B^{(k)}(T_b, n_{\mathrm{g}}), \qquad k = 1, \ldots, N, \tag{2.11}$$

where the integrals r_1 and r_2 are defined by

$$r_1 = \int_0^1 \mu \rho(-\mu) d\mu, \qquad\qquad r_2 = \int_0^1 \mu^2 \rho(-\mu) d\mu.$$

In summary, the SP_1 approximation of the RHT problem (2.9) can be reformulated as

$$\begin{aligned}
\frac{\partial T}{\partial t} - \nabla\cdot\big(k_c\nabla T\big) &= \sum_{k=1}^{N}\nabla\cdot\Big(\frac{1}{3\kappa_k}\nabla\varphi^{(k)}\Big), && (\mathbf{x},t)\in\Omega\times[0,t_{end}),\\
-\nabla\cdot\Big(\frac{\varepsilon^2}{3\kappa_k}\nabla\varphi^{(k)}\Big)+\kappa_k\varphi^{(k)} &= 4\pi\kappa_k B^{(k)}(T,n_{\rm g}), && (\mathbf{x},t)\in\Omega\times[0,t_{end}),\\
\varepsilon k_c\mathbf{n}(\hat{\mathbf{x}})\cdot\nabla T + h_c(T-T_b) &= \alpha\pi\Big(B^{(0)}(T_b,n_{\rm b})-B^{(0)}(T,n_{\rm b})\Big), && (\hat{\mathbf{x}},t)\in\partial\Omega\times[0,t_{end}),\\
\varphi^{(k)}+\left(\frac{1+3r_2}{1-2r_1}\frac{2\varepsilon}{3\kappa_k}\right)\mathbf{n}(\hat{\mathbf{x}})\cdot\nabla\varphi^{(k)} &= 4\pi B^{(k)}(T_b,n_{\rm g}), && (\hat{\mathbf{x}},t)\in\partial\Omega\times[0,t_{end}),\\
T(\mathbf{x},0) &= T_0(\mathbf{x}), && \mathbf{x}\in\Omega,
\end{aligned}\tag{2.12}$$

for $k=1,2,\ldots,N$. Note that the SP_1 approximation (2.12) consists to solve a system of $(N+1)$ coupled semi-linear elliptic-parabolic equations. It should also be stressed that the enriched partition of unity finite element method proposed in the current study can also be extended to the SP_2 and SP_3 approximations from [10] without major conceptual modifications.

3 Time discretization approach

To integrate the equations (2.12) we divide the time interval $[0,t_{end})$ into equi-distributed subintervals $[t_n,t_{n+1}]$ with length $\Delta t = t_{n+1}-t_n$ for $n=0,1,\ldots$. We use the notation W_n to denote the value of a generic function W at time t_n. Hence, applying to the system (2.12) a linearly implicit time stepping scheme results in

$$\begin{aligned}
\frac{T_{n+1}-T_n}{\Delta t} - \nabla\cdot\big(k_c\nabla T_{n+1}\big) &= \sum_{k=1}^{N}\nabla\cdot\Big(\frac{1}{3\kappa_k}\nabla\varphi^{(k)}\Big),\\
-\nabla\cdot\Big(\frac{\varepsilon^2}{3\kappa_k}\nabla\varphi^{(k)}\Big)+\kappa_k\varphi^{(k)} &= 4\pi\kappa_k B^{(k)}(T_n,n_{\rm g}), \qquad k=1,2,\ldots,N,\\
\varepsilon k_c\mathbf{n}(\hat{\mathbf{x}})\cdot\nabla T_{n+1} + h_c(T_{n+1}-T_b) &= \alpha\pi\Big(B^{(0)}(T_b,n_{\rm b})-B^{(0)}(T_n,n_{\rm b})\Big),\\
\varphi^{(k)}+\left(\frac{1+3r_2}{1-2r_1}\frac{2\varepsilon}{3\kappa_k}\right)\mathbf{n}(\hat{\mathbf{x}})\cdot\nabla\varphi^{(k)} &= 4\pi B^{(k)}(T_b,n_{\rm g}), \qquad k=1,2,\ldots,N,\\
T^0(\mathbf{x}) &= T_0(\mathbf{x}).
\end{aligned}\tag{3.1}$$

Note that the mean radiative intensity $\varphi^{(k)}$ does not depend explicitly on the time variable, however its dynamics depend on the time evolution of the medium temperature. Thus, one could replace the mean radiative intensity $\varphi^{(k)}$ in (3.1) by $\varphi^{(k)}_{n+1}$ to emphasize its implicit dependence on the time. The procedure to advance the solution from the time t_n to the next time t_{n+1} can be carried out in the following two steps:

Step 1. Radiation stage: For $k=1,2,\ldots,N$, solve for $\varphi^{(k)}_{n+1}$

$$\begin{aligned}
-\nabla\cdot\Big(\frac{\varepsilon^2}{3\kappa_k}\nabla\varphi^{(k)}_{n+1}\Big)+\kappa_k\varphi^{(k)}_{n+1} &= 4\pi\kappa_k B^{(k)}(T_n,n_{\rm g}),\\
\varphi^{(k)}_{n+1}+\left(\frac{1+3r_2}{1-2r_1}\frac{2\varepsilon}{3\kappa_k}\right)\mathbf{n}(\hat{\mathbf{x}})\cdot\nabla\varphi^{(k)}_{n+1} &= 4\pi B^{(k)}(T_b,n_{\rm g}).
\end{aligned}\tag{3.2}$$

Step 2. Conduction stage: Solve for T_{n+1}

$$\begin{aligned}
\frac{T_{n+1}-T_n}{\Delta t} - \nabla\cdot\big(k_c\nabla T_{n+1}\big) &= \sum_{k=1}^{N}\nabla\cdot\Big(\frac{1}{3\kappa_k}\nabla\varphi_{n+1}^{(k)}\Big),\\
\varepsilon k_c\mathbf{n}(\hat{\mathbf{x}})\cdot\nabla T_{n+1} + h_c(T_{n+1}-T_b) &= \alpha\pi\Big(B^{(0)}(T_b,n_{\rm b}) - B^{(0)}(T_n,n_{\rm b})\Big), \qquad (3.3)\\
T^0(\mathbf{x}) &= T_0(\mathbf{x}).
\end{aligned}$$

For the sake of simplicity we rewrite equations (3.2) and (3.3) in a compact form as

$$u - \nabla\cdot\big(\mathcal{E}\nabla u\big) = F, \qquad \text{in} \quad \Omega, \qquad (3.4a)$$

$$u + \beta\mathbf{n}(\hat{\mathbf{x}})\cdot\nabla u = f, \qquad \text{on} \quad \partial\Omega, \qquad (3.4b)$$

where, for the mean radiative intensities $u=\varphi_{n+1}^{(k)}$, $k=1,2,\ldots,N$,

$$\mathcal{E}=\frac{\varepsilon^2}{3\kappa_k^2}, \qquad F=4\pi B^{(k)}(T_n,n_{\rm g}), \qquad \beta=\frac{1+3r_2}{1-2r_1}\frac{2\varepsilon}{3\kappa_k}, \qquad f=4\pi B^{(k)}(T_b,n_{\rm g}).$$

For the temperature field $u=T_{n+1}$

$$\mathcal{E}=k_c\Delta t, \qquad F=T_n+\sum_{k=1}^{N}\nabla\cdot\Big(\frac{\Delta t}{3\kappa_k}\nabla\varphi_{n+1}^{(k)}\Big), \qquad \beta=\frac{\varepsilon k_c}{h_c}, \qquad f=T_b+\frac{\alpha\pi}{h_c}\Big(B^{(0)}(T_b,n_{\rm b})-B^{(0)}(T_n,n_{\rm b})\Big).$$

It is worth remarking that, to avoid the evaluation of the gradient in the right-hand side F, we use the second equation in (3.1) to obtain

$$F=T_n+\sum_{k=1}^{N}\kappa_k\frac{\Delta t}{\varepsilon^2}\left(\varphi_{n+1}^{(k)}-4\pi B^{(k)}(T_n,n_{\rm g})\right).$$

Note that the above time integration scheme is only first-order accurate and conditionally stable. Other high-order linearly implicit methods can also be applied. In the solution procedure, only linear systems have to be solved at each time step to update the temperature T_{n+1} and the mean radiative intensities $\varphi_{n+1}^{(k)}$. We should also point out that the source term in (3.2) contains the explicit temperature variable T_n. It is possible to treat this term implicitly by solving first the conduction stage followed by the radiation stage. In the considered test examples, both treatments produce the same results. Another way to solve the above equations is to involve all the stages implicitly in time and solve one single system of the form (3.4) for $U=\Big(T_{n+1},\varphi_{n+1}^{(1)},\varphi_{n+1}^{(2)},\ldots,\varphi_{n+1}^{(N)}\Big)^T$. This procedure results in a large, coupled and nonlinear system of algebraic equations to be solved at each time step. However, the numerical solution of such nonlinear system is computationally demanding and it may limit the efficiency of the algorithm.

4 Variational formulation

Since the spatial discretization approach is based on the finite element method, a variational formulation of the problem is established for the problem (3.4). We consider the Sobolev space $H^1(\Omega)$ which denotes the set of square integrable functions whose first derivatives are also square integrable. The weak variational formulation of the problem can be described as: Find $u\in H^1(\Omega)$ such that

$$\mathbf{a}(u,v)=\mathbf{b}(v), \qquad \forall v\in H^1(\Omega), \qquad (4.1)$$

where v is a test function in $H^1(\Omega)$, $\mathbf{a}$ and $\mathbf{b}$ are bilinear and linear forms defined respectively, as

$$\mathbf{a}(u,v) = \int_\Omega vud\mathbf{x} - \int_\Omega \mathcal{E}v\nabla^2 ud\mathbf{x}, \qquad \mathbf{b}(v) = \int_\Omega vFd\mathbf{x}. \tag{4.2}$$

Using the divergence theorem, the bilinear form results in

$$\mathbf{a}(u,v) = \int_\Omega \Big(\mathcal{E}\nabla v\cdot\nabla u + v\ u\Big)d\mathbf{x} - \oint_{\partial\Omega} \mathcal{E}v\nabla u\cdot\mathbf{n}d\hat{\mathbf{x}}. \tag{4.3}$$

After substitution of the boundary condition (3.4b) into (4.3) the bilinear form reads

$$\mathbf{a}(u,v) = \int_\Omega \Big(\mathcal{E}\nabla v\cdot\nabla u + v\ u\Big)d\mathbf{x} + \oint_{\partial\Omega} \frac{\mathcal{E}}{\beta}v\Big(u-f\Big)d\hat{\mathbf{x}}. \tag{4.4}$$

Let the domain Ω be partitioned into N_e non-overlapping sub-domains Ω^m, $m = 1,\ldots,N_e$. Each sub-domain, or finite element in the engineering terminology, is given through a coordinate transformation $\mathbf{x} = L^k(\boldsymbol{\eta})$ between the real space and the local system $\boldsymbol{\eta} = (\eta_1,\eta_2) \in \mathcal{L}$. The used elements are of triangular type with $\mathcal{L} = \mathcal{T}\times[-1,1]$ where $\mathcal{T}$ stands for the triangular domain

$$\mathcal{T} = \Big\{\eta_1 \geq 0, \quad \eta_2 \geq 0, \quad \eta_1+\eta_2 \leq 1\Big\}. \tag{4.5}$$

Using a conventional piecewise finite element space, the solution u on Ω^m is approximated as

$$u \simeq u_h^m = \sum_{p=1}^{\#\text{vert}} \mathcal{N}_p(\boldsymbol{\eta})u_p^m, \tag{4.6}$$

where $\mathcal{N}_p$ stands for the (P_1) Lagrangian polynomial on $\mathcal{L}$ and u_p are the nodal values corresponding to the vertices of $\mathcal{L}$ with $\#\text{vert} = 3$ for the triangular type elements used here. The approximation (4.6) requires the mesh size to be small enough to capture the variable field. This limitation is to be alleviated if a set of local enrichment functions are included, see for example [18, 17].

5 Approximation by field-enriched finite elements

In order to achieve better approximation properties than is allowed by the polynomial basis functions $\mathcal{N}_p$ we use the partition of unity method [14] to enrich the solution space with hyperbolic basis functions. It was found that for problems of steep boundary layers using enrichments with steep gradients can significantly improve the approximation of the finite element approach [18]. For example in a polygonal domain and for an edge e, at a position $x = x_e$, the enrichment functions may be written as

$$\overline{G}_{qe} = C_1 + C_2\tanh\left(\frac{x-x_e}{h_q}\right), \qquad q = 1,2,\ldots,Q, \tag{5.1}$$

where C_1 and C_2 are constants defining the amplitude of the enrichment jump while h_q is the parameter to control the steepness of the function $\overline{G}_{qe}$. The same functions can be used as well for a circular edge $r = r_e$ using polar coordinates (r,θ) by replacing x and x_e with r and r_e, respectively. Similar enrichment functions can be reconstructed for elliptical geometries using elliptical coordinates. Such families of functions may be written for all appropriate edges forming the boundary $\partial\Omega$. Then the enrichment functions considered in this paper are summed over all edges at which boundary layers may develop, *i.e.* the family of these enrichment functions to be introduced into the analysis is

$$G_q = \sum_{e=1}^{\#\text{edges}} \overline{G}_{qe}, \qquad q = 1,2,\ldots,Q \tag{5.2}$$

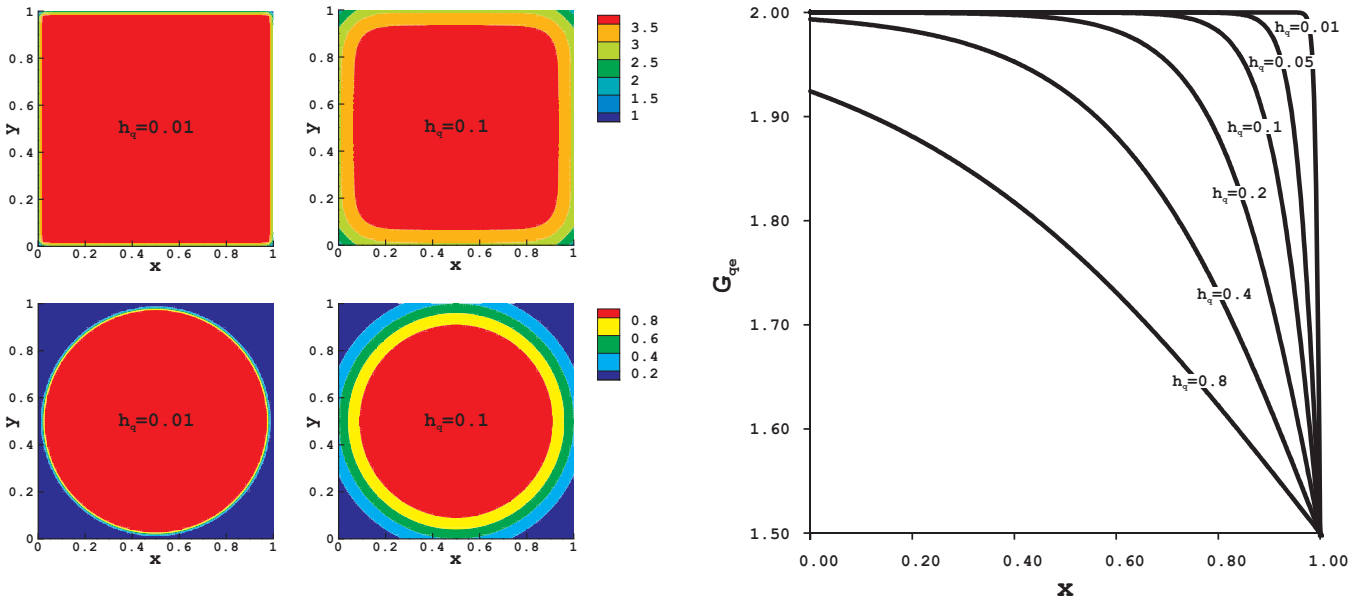

Figure 5.1: Illustration of enrichment functions of different orders used in the present study. Planar view of hyperbolic tangent functions (left) and the associated cross-sections for different values of h_q (right).

In Figure 5.1 we illustrate the change in the enrichment for different values of h_q. The figure also shows the enrichment functions for the four edges of a squared domain and a circular edge of a disc. As illustrated in Figure 5.1 the key component in the enrichment functions is the choice of h_q. In the RHT problems considered here, the thermal gradients can vary from infinity, at the start of the cooling, to zero at the steady state. Thus h_q is chosen such that the first enrichment function is of the highest gradient allowed by the machine precision. Similarly the last enrichment function is chosen to be of a gradient close to zero. For the simulations presented in the current study, the values of h_q range from $h_q = 0.01$ to $h_q = 1$. Then the intermediate functions are designed such that they are of decreasing gradient. The difference in the gradient between any pair of successive enrichments is limited by two factors. First the difference should be small enough to enable smooth recovery of the entire time history. In other words, it is possible to approximate the solution gradient at any simulation time using one or a combination of these functions. The second limitation is related to the numerical stability because two successive enrichment functions may become indistinguishable from the numerical point of view, if the difference between them is too small to be observed by the given accuracy (double precision here). Hence, the linear system resulting from such enrichment would be highly ill-conditioned or even singular. It should also be stressed that, although this variation in h_q represents the temporal behaviour of the solution, h_q itself remains time independent. This is an important feature of the considered enrichment in order to keep the shape functions independent of time. More details about the choice of the enrichment functions can be found in [18, 17].

The enrichment functions G_q are used within the partition of unity framework to express the nodal values u_p at any time $t = t_n$ as

$$u_p^n = \sum_{q=1}^{Q} A_p^{q,n} G_q. \tag{5.3}$$

Here the element number m is dropped for ease of notation. Thus the new unknowns to be computed by solving the finite element resulting linear system are $A_p^{q,n}$, for $q = 1, 2, \dots Q$, which may be defined as the contribution of each enrichment function G_q to the nodal value u_p^n at the node p. Using expression (5.3), the solution u_h^n identified in expression (4.6) can be rewritten as

$$u_h^n = \sum_{p=1}^{\#\text{vert}} \sum_{q=1}^{Q} A_p^{q,n} \mathcal{N}_p G_q. \tag{5.4}$$

Table 5.1: Absorption coefficients for the eight frequency bands used in our simulations.

band k	ν_{k-1} $[10^{13}s^{-1}]$	ν_k $[10^{13}s^{-1}]$	λ_k $[\mu m]$	λ_{k-1} $[\mu m]$	κ_k $[m^{-1}]$
-	0	2.933	7.00	∞	opaque
1	2.933	3.422	6.0	7.0	7136.00
2	3.422	3.733	5.5	6.0	576.32
3	3.733	4.563	4.5	5.5	276.98
4	4.563	5.133	4.0	4.5	27.98
5	5.133	5.866	3.5	4.0	15.45
6	5.866	6.844	3.0	3.5	7.70
7	6.844	102.671	0.2	3.0	0.50
8	102.671	∞	0.0	0.2	0.40

Table 5.2: Reference parameters considered in the present work for glass cooling process.

Glass density	$\rho_g = 2514.8\ kg/m^3$
Specific heat capacity	$c_g = 1239.6\ J/kgK$
Speed of light in vacuum	$c_0 = 2.9979 \times 10^8\ m/s$
Plank constant	$h_P = 6.62608 \times 10^{-34}\ Js$
Boltzmann constant	$k_B = 1.38066 \times 10^{-23}\ J/K$
Thermal conductivity	$k_c = 1.672\ Wm/K$
Convective heat transfer	$h_c = 0.001$
Hemispheric emissivity	$\alpha = 0.92$
Refractive index of air	$n_{\mathrm{b}} = 1$
Refractive index of glass	$n_{\mathrm{g}} = 1.46$
Initial temperature	$T_0 = 1000\ K$
Ambient temperature	$T_b = 300\ K$

It should be stressed that, the proposed enrichment functions are time-independent and written in a global form but modulated locally on an element level through the conventional shape functions $\mathcal{N}_p$. Based on the order of these shape functions either linear or quadratic, a combination of the enrichment functions are used to approximate the solution of the considered problems. Although the functions are time-independent, the time dependency aspect of the problem is included in these combinations of functions. To express the time dependency in this manner together with the linearly implicit time integration scheme presented here leads to the ability of retaining the system matrix, assembled at the first time step, to be reused at later time steps without alteration. In addition, the computations required to solve the linear system can also be reduced which can be achieved in different ways. In the present work we opt to solve the linear system using an $\mathsf{LDL}^\top$ decomposition where L is a lower and D is a diagonal matrix, see for instance [1]. Thus, it only requires to decompose the matrix in the system at the first time step and then, after updating the right-hand side of the linear system, one only applies a forward, diagonal and back substitutions to obtain the solution at any time step. This significantly increases the efficiency when a large number of time steps is needed, compared to updating the matrix and solving the problem at every time step.

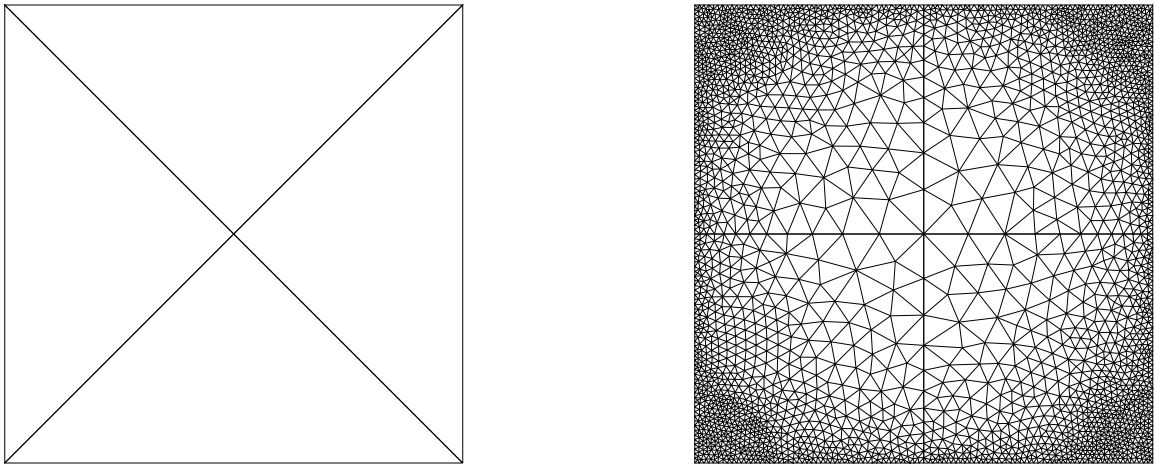

Figure 5.2: Comparison between the PUFEM mesh (left) and the coarse FEM mesh (right) for the test example of glass cooling in a plate enclosure.

6 Numerical results and applications

In this section we present numerical results for two test examples in the glass cooling process. The focus is on examining the numerical performance of the PUFEM algorithm described above and comparing its efficiency to the standard FEM. In the first example, the PUFEM solution is also compared to the solution obtained using the FDM and the full radiative heat transfer model. In both examples, the enrichment is applied on elements of the same order as in the FEM being compared against, that is linear elements for the first example and quadratic elements for the second example. The presented results for cooling of a glass plate in the first example and a glass disc in the second, can be typical fabrication steps in glass manufacturing. The non-opaque frequency interval $[\nu_0, \infty)$ is approximated by an eight-band model studied in [10, 8]. Since the data are originally defined by wavelength intervals $[\lambda_{k-1}, \lambda_k]$, we computed the corresponding frequency bands using the relation

$$\nu_k = \frac{c_0}{\lambda_k \, n_g}.$$

The considered eight wavelength bands and their associated frequencies and absorption coefficients are listed in Table 5.1. It is evident from this table that the material is non-grey and the optical properties strongly change with the wavelength. In addition, the glass is considered to be opaque to radiation for wavelengths larger than a cut-off wavelength equal to 7 μm. In all the computations reported herein, we used data listed in Table 5.2. In this study we highlight the effect of an instantaneous change in the ambient temperature from 1000 K to 300 K, causing a sharp drop in the temperature across a boundary layer that can be very thin depending on the physical properties of the enclosure.

In the current study, to evaluate elementary matrix entries all the integrals are evaluated numerically using the standard Gaussian quadrature. A high number of integration points is chosen with the PUFEM such that the results are not affected by the integration errors. However, the total number of points used with the PUFEM remains smaller than with the FEM models due to the much higher number of elements with the FEM. The resulting linear systems of algebraic equations are solved using a direct solver.

6.1 Glass cooling in a plate enclosure

As a first test example we consider a unit glass square. Two different optical regimes are considered, corresponding to two different values of the non-dimensional parameter $\varepsilon = 0.5$ and $\varepsilon = 1$. Relatively large values of ε are selected in this study in order to consider optically thin regimes where the effect of radiation is more pronounced. For optically thick regimes, the results obtained using the simplified P_1

Table 6.1: Mesh statistics for the meshes used in the FEM for glass cooling in a plate enclosure.

	Mesh A	Mesh B	Mesh C	Mesh D
Number of nodes	2947	11389	44761	177457
Number of elements	5496	21984	87936	351744

approximation and the full radiative transfer model demonstrate good agreements, see for example [10]. The aim in this example is to conduct a comparative study of the performance of the proposed PUFEM to that of the conventional h-version FEM with the latter being the usual approach used in glass manufacturing. First, for the FEM solution we mesh the domain into linear three-noded elements where fine elements are used close to the domain boundary as shown in the right plot in Figure 5.2. Starting with this mesh we progressively refine it by connecting the midpoints of each element to subdivide it into four smaller elements. Three refinement procedures are applied to create three more meshes. The statistics of the four meshes are summarized in Table 6.1. For the PUFEM we use a very coarse mesh with only five nodes and four linear three-noded elements as shown in the left plot in Figure 5.2. The PUFEM is also enriched using five hyperbolic functions (*i.e.* $Q = 5$) making its total number of degrees of freedom 25 which is still a tiny fraction of the corresponding number with the coarsest finite element mesh which is 2947. We retain the same PUFEM mesh as well as the same enrichment for solving the eight radiative mean intensities $\varphi^{(k)}$ ($k = 1, 2 \ldots, 8$) and the temperature T. This is an equivalent to the usual procedure, which is followed here, of retaining the same finite element mesh when solving conduction-radiation problems. In order to assess the accuracy of the considered PUFEM and the FEM with respect to the time integration scheme we run the simulations using three different time steps namely, $\Delta t = 10^{-6}$, 10^{-7} and 10^{-8}.

We first evaluate the accuracy of the PUFEM and the FEM for resolving the boundary layers for the cooling case with the optical scale $\varepsilon = 0.5$. In Figure 6.1 we present the temperature variation along the domain edge ($y = 0$) at different simulation times using the considered meshes. Similar plots for the cooling case but with $\varepsilon = 1$ are displayed in Figure 6.2. In each plot in these figures, the temperature at the domain edge is depicted for the three considered timestep sizes. Note that for a given simulation time, the number of time steps for $\Delta t = 10^{-6}$ is 10 times and 100 times the number of time steps for $\Delta t = 10^{-7}$ and for $\Delta t = 10^{-8}$, respectively. It is evident in both figures that the FEM solution at early simulation times and with coarser meshes, exhibits strong oscillations that are reduced by refining the mesh. Independently of the mesh refinement, these oscillations damp out at later simulation times. An interesting observation is that the pattern of these oscillations seems to be unaffected by the timestep size or the diffusion scale ε. For instance, the boundary pattern found in Mesh A seems similar to the one found in Mesh B but with different amplitudes. Even for the fine meshes Mesh C and Mesh D at the simulation time $t = 2 \times 10^{-6}$, the temperature seems to have small amplitude counterparts to the major spikes found in the results obtained for the coarse Mesh A. This may be attributed to the fact that each of these meshes is a subset of another through its refinement. In comparison with the PUFEM solutions, it is clear that these spurious boundary oscillations are absent in the results obtained using the PUFEM.

It is also clear from the results presented in Figure 6.1 and Figure 6.2 that the simulations with the time step $\Delta t = 10^{-7}$ overlap those obtained using $\Delta t = 10^{-8}$ for all simulation times. A small discrepancy between the results obtained using $\Delta t = 10^{-6}$ and other time steps can also been detected at early simulation times. The FEM solution on coarse meshes seems to be less sensitive to the selection of the time step Δt. This is to be expected as the space discretization error dominates the global error whereas on finer meshes the error in the time discretization becomes more dominant. Similarly, the PUFEM solution shows sensitivity to the selection of the time step like the FEM solution on finer meshes. As the simulation time increases, this sensitivity with respect to Δt in both methods becomes negligible. However, the PUFEM still shows sensitivity at the time $t = 4 \times 10^{-6}$ for $\varepsilon = 0.5$ and at time $t = 8 \times 10^{-6}$ for $\varepsilon = 1$, unlike the FEM on the fine Mesh D, which seems to be less sensitive at the respective time. Bearing in mind the slight change in the results obtained using $\Delta t = 10^{-7}$ and $\Delta t = 10^{-8}$ at the expense of rather significant increase in

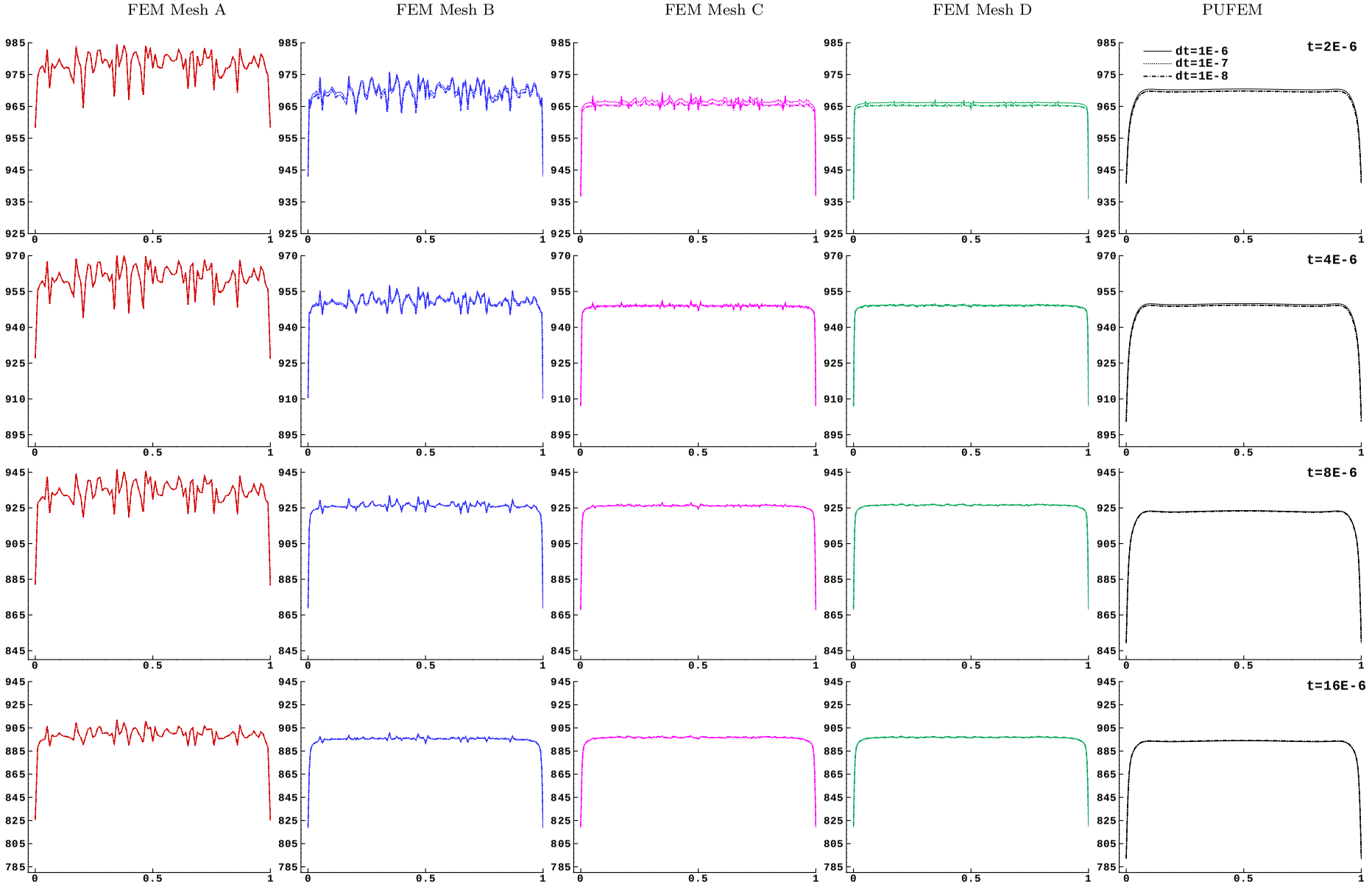

Figure 6.1: Comparison of the temperature along the domain edge ($y = 0$) using different timesteps for the PUFEM and the FEM on different meshes at time $t = 2 \times 10^{-6}$ (first row), 4×10^{-6} (second row), 8×10^{-6} (third row) and 16×10^{-6} (fourth row) for $\varepsilon = 0.5$. The results are shown for the FEM on Mesh A (first column), FEM on Mesh B (second column), FEM on Mesh C (third column), FEM on Mesh D (fourth column) and the PUFEM (fifth column).

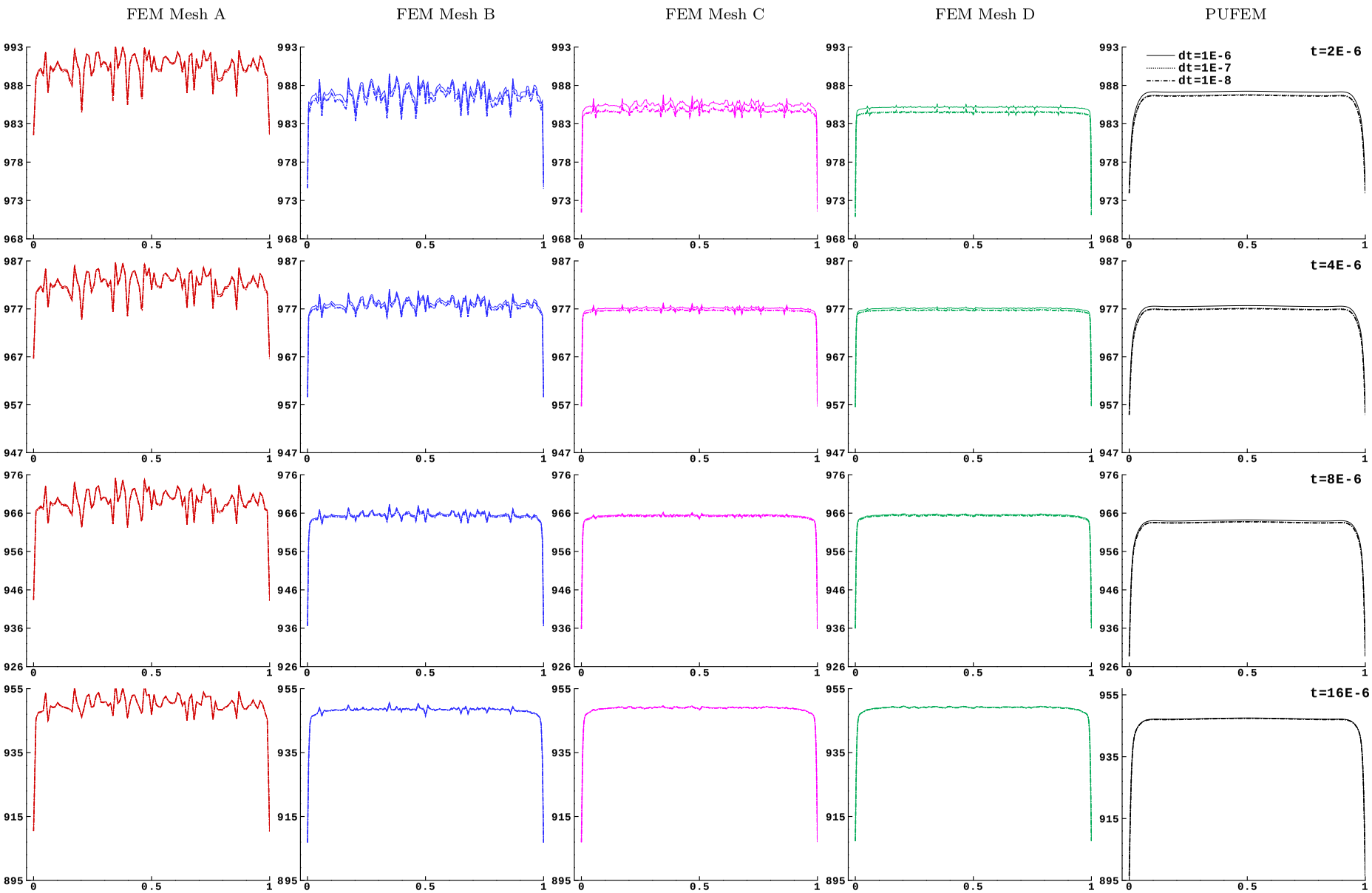

Figure 6.2: The same as Figure 6.1 but for $\varepsilon = 1$

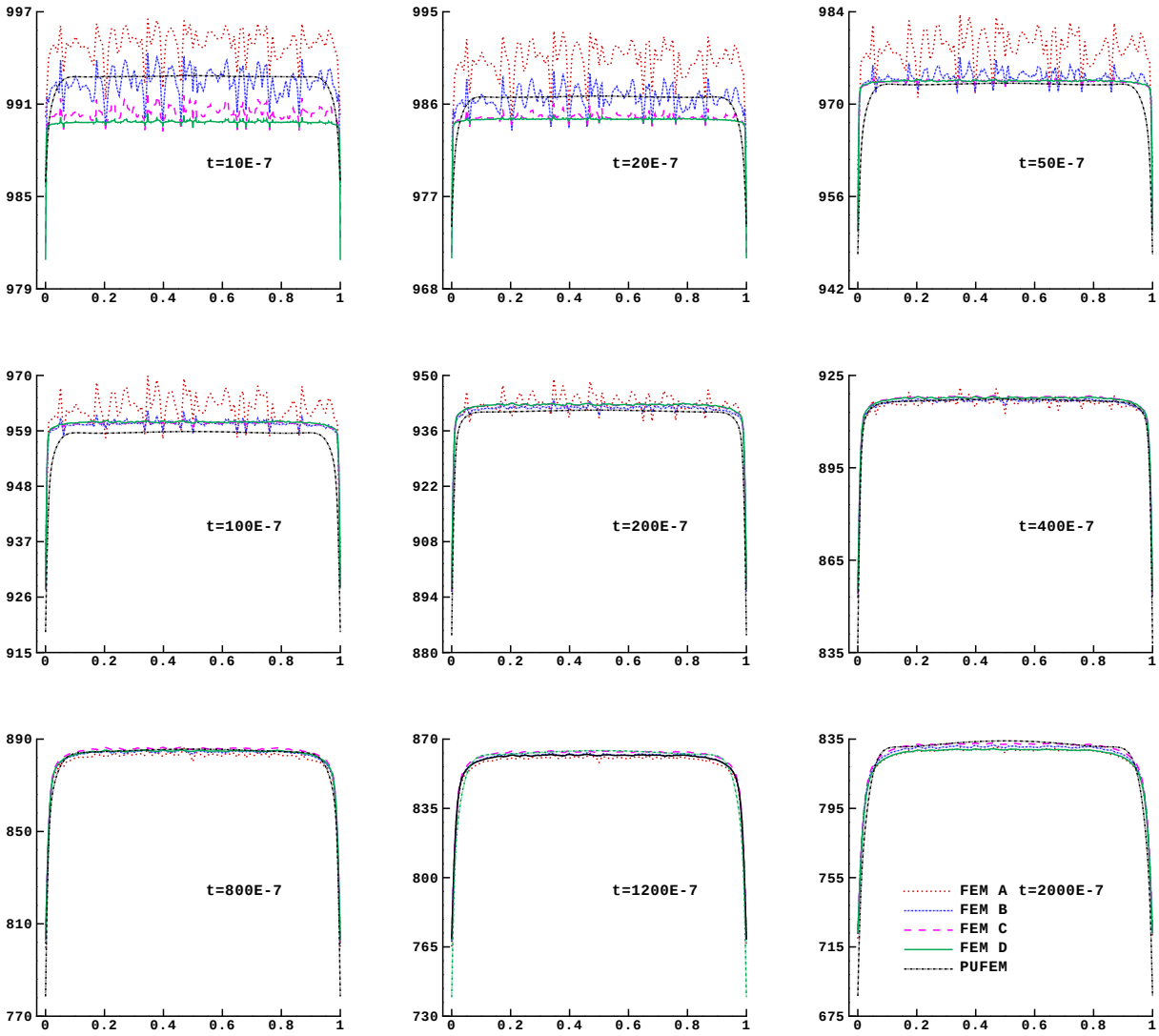

Figure 6.3: Comparison of the recovered temperature along the domain edge ($y = 0$) using the FEM on the four considered meshes and the PUFEM at different instants with $\varepsilon = 1$.

CPU times, the time step $\Delta t = 10^{-7}$ is believed to be adequate to obtain numerical results free of time integration effects. Hence, the results presented hereafter are based on using $\Delta t = 10^{-7}$.

To further investigate the effect of the FEM meshes on the resolution of boundary layers, Figure 6.3 illustrates the temperature variation along the domain edge ($y = 0$) at different simulation times where the four considered FEM meshes and the PUFEM are included in the same plots for a better insight. Only results obtained using $\varepsilon = 1$ are displayed in this figure whereas numerical results using $\varepsilon = 0.5$ not reported here, exhibit similar features. Note that the selected simulation times are considered in order to compare the temperature features on the domain edge obtained using the FEM on different meshes to those obtained using the PUFEM on the very coarse mesh shown in Figure 5.2 by keeping the time step fixed to $\Delta t = 10^{-7}$. As in the previous simulations, the oscillations in the FEM results on the coarse meshes are noted where the correspondence between spikes of different meshes can be easily recognized. The plots at early instants consistently show the average edge temperature as predicted by the coarse FEM meshes is higher than that predicted by the fine FEM meshes. The oscillations in the temperature results obtained using the FEM on Mesh C are damped out first, then followed by Mesh B and at later times by Mesh A as all the three

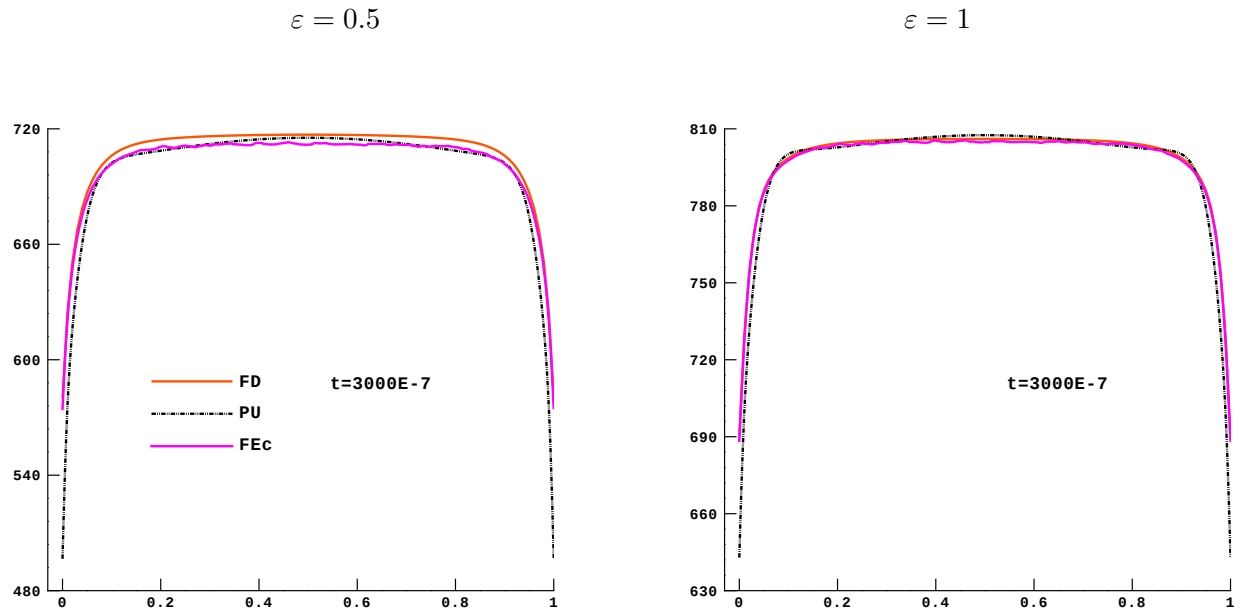

Figure 6.4: Comparison of the temperature along the domain edge ($y = 0$) using FDM, PUFEM and FEM on Mesh C for the example of glass cooling in a plate enclosure at $\varepsilon = 0.5$ (left) and $\varepsilon = 1$ (right).

converge toward the results obtained using the FEM on Mesh D. In comparison, the PUFEM results seem to start at a higher temperature before converging towards the FEM on Mesh D in a similar manner to the coarser finite element meshes. However, some oscillations in time evolution are observed here, where the PUFEM starts higher then becomes lower before becoming close to those obtained using the FEM on Mesh D; finally it seems slightly at a higher temperature than the FEM on Mesh D. As the solution evolves in time, a significant difference in temperature at the domain corners is observed between the FEM and the PUFEM which may be expected due to the singularities at the domain corners. To further investigate, Figure 6.4 compares the PUFEM solution after 3000 timesteps to the solution on Mesh C using $\Delta t = 10^{-7}$. In the same figure we include the results obtained using the canonical FDM on a uniform mesh of 100×100 gridpoints for $\varepsilon = 0.5$ and $\varepsilon = 1$. The presented results show a close agreement of the solutions obtained along the edge using the FEM, the PUFEM and the FDM except in the corners where the PUFEM again predicts a lower temperature. The close resemblance between the results obtained using different methods suggests that the previous conclusion of the FEM on different meshes and the PUFEM on the coarse mesh converging to the same solution as the problem loses its heat energy is correct. It should be noted here that despite its established accuracy in solving this type of problems [10], the FDM is strictly limited by the geometry of computational domains under study. Furthermore, the necessity of including process across a range of spatial scales means that techniques capable of operating on unstructured meshes will be more appropriate than those such as the FDM which rely on structured and often regular meshes. Therefore the use of the FDM is uncommon for industrial applications where usually the FEM is the method of choice.

Our next concern with this example is to compare the results obtained using the PUFEM for the simplified P_1 model (2.12) to those from a direct solver for the full radiative heat transfer equations (2.7). To this end we solve the RHT equations (2.7) using the well-established Diffusion Synthetic Acceleration (DSA) method. The DSA method uses the diffusion approach to accelerate the source iteration which has been widely used in computational radiative transfer. We refer to [25, 24] for the implementation of the method and further discussions on other direct methods for RHT problems can be found therein. The S_8 discrete-ordinate algorithm (with 80 directions) is selected for the discretization of the angle variable and a mesh of 100×100 gridpoints is used in our computations, yielding a linear system with 64×10^5 unknowns which has to be solved for each time step. Here, we also consider the canonical Rosseland approach widely

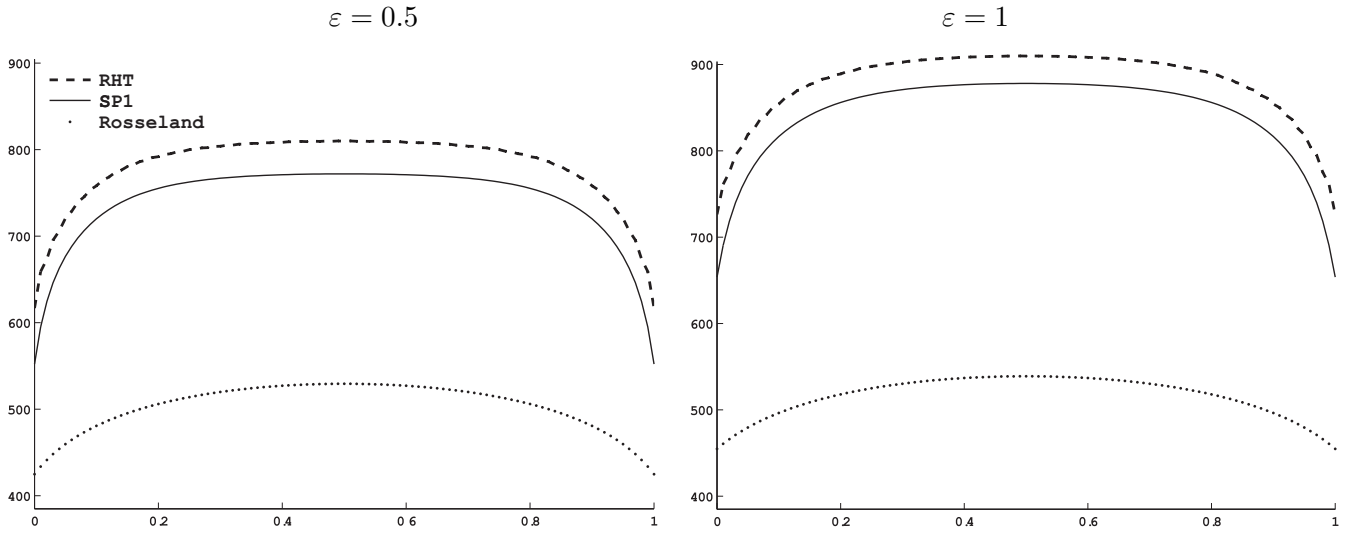

Figure 6.5: Cross section of the temperature at ($y = 0.5$) obtained using the RHT, Rosseland and PUFEM models for $\varepsilon = 0.5$ (left) and $\varepsilon = 1$ (right) at time $t = 2 \times 10^{-3}$ for the glass cooling in a plate enclosure.

used in glass cooling. This approach consists of replacing the RHT equations (2.9) by the following diffusion problem

$$\begin{aligned} \frac{\partial T}{\partial t} - \nabla \cdot \Big(\big(k_c + k_r(T)\big) \nabla T \Big) &= 0, && (\mathbf{x}, t) \in \Omega \times (0, t_{end}], \\ \varepsilon k_c \mathbf{n}(\hat{\mathbf{x}}) \cdot \nabla T + h_c (T - T_b) &= \alpha\pi \Big(B^{(0)}(T_b, n_{\rm b}) - B^{(0)}(T, n_{\rm b}) \Big), && (\hat{\mathbf{x}}, t) \in \partial\Omega \times [0, t_{end}), \\ T(\mathbf{x}, 0) &= T_0(\mathbf{x}), && \mathbf{x} \in \Omega, \end{aligned} \tag{6.1}$$

where the conduction coefficient $k_r(T)$ is given by

$$k_r(T) = \frac{4\pi}{3} \int_{\nu_0}^{\infty} \kappa(\nu) \frac{\partial B(T, \nu, n_{\rm g})}{\partial T} d\nu.$$

Comparisons between the computed results obtained for the RHT problem (2.9), the SP_1 approximation (2.12) and the Rosseland model (6.1) are shown in Figure 6.5. Here, cross sections of the temperature at the main horizontal axis ($y = 0.5$) are displayed at time $t = 2 \times 10^{-3}$ for both optical regimes considered $\varepsilon = 0.5$ and $\varepsilon = 1$. As expected, accounting for radiation in the computational analysis by the SP_1 model has produced better agreement between the predicted temperature using the SP_1 approximation and the full RHT problem. The classical Rosseland model poorly underestimates the glass cooling and it fails to resolve the boundary layers in the temperature field at both $\varepsilon = 0.5$ and $\varepsilon = 1$. However, the domain temperature is better approximated with Rosseland model for smaller values of ε. This is due to the influence of radiation on the temperature profile where for a smaller ε the radiation effect is reduced *i.e.*, the medium becomes more optically thick. This also shows that the inclusion of thermal radiation in the glass cooling has significantly changed the temperature profile in the enclosure for both RHT and SP_1 but not for Rosseland. More details may be found in [24] where extensive comparisons for SP_N approximations using different values of ε were performed in. If the effect of radiation is to be considered in the cooling analysis the predictions by SP_1 is much closer to that of RHT models and provide further improvements over the Rosseland model in the domain temperature as well as in the boundary layers profile. As efficiency is usually important in the development of glass simulating codes, the PUFEM for solving the SP_1 model proposed in this paper is not only realistic enough to yield meaningful predictions, but also simple and fast enough to avoid overcharging the computational cost.

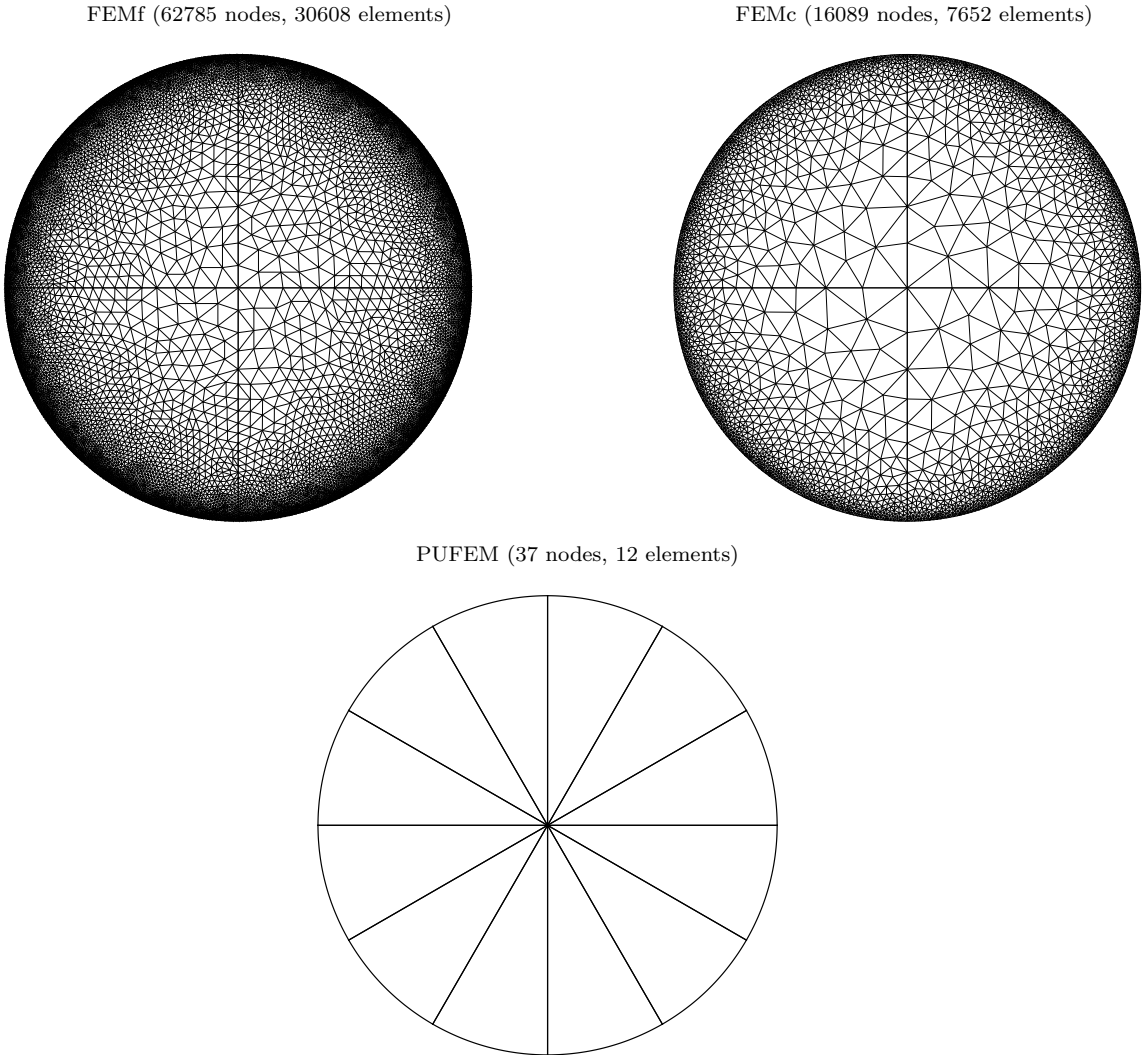

Figure 6.6: Comparison between the FEM meshes (top) and the PUFEM mesh (bottom).

6.2 Glass cooling in a disc enclosure

In this test example we consider the annealing of a glass disc with unit radius. The thermodynamical and optical properties of the material are the same as in the previous example taken from Table 5.2. The objectives of this example are twofold: (i) to verify the performance of the PUFEM compared to the conventional FEM for the circular geometry, in terms of accuracy and efficiency when dealing with boundary layers, and (ii) to investigate a refined enrichment procedure in which the number of enrichment functions Q used varies with the eight frequency bands. By considering this type of adaptive enrichment we expect to obtain a significant reduction in the overall computational cost since the number of degrees of freedom would vary for each band according to the associated absorption coefficient. We refer to this procedure by q-refinement, as opposed to the well-established h-refinement where the FEM mesh is adapted according to a measured error indicator. In the q-refinement, the PUFEM mesh remains the same during the simulation process and only the number of enrichment functions Q in (5.3) is allowed to vary for each frequency band. For the FEM simulations we consider two meshes (a coarse mesh referred to as FEMc and a fine mesh referred to as FEMf) which are presented in Figure 6.6. In this figure we also include the mesh used in our simulations using the PUFEM. We emphasize the extremely low number of elements and nodes listed in Figure 6.6 for the PUFEM mesh compared to both the coarse and the fine FEM meshes.

It should be noted here that this glass cooling problem can also be solved as in the previous test

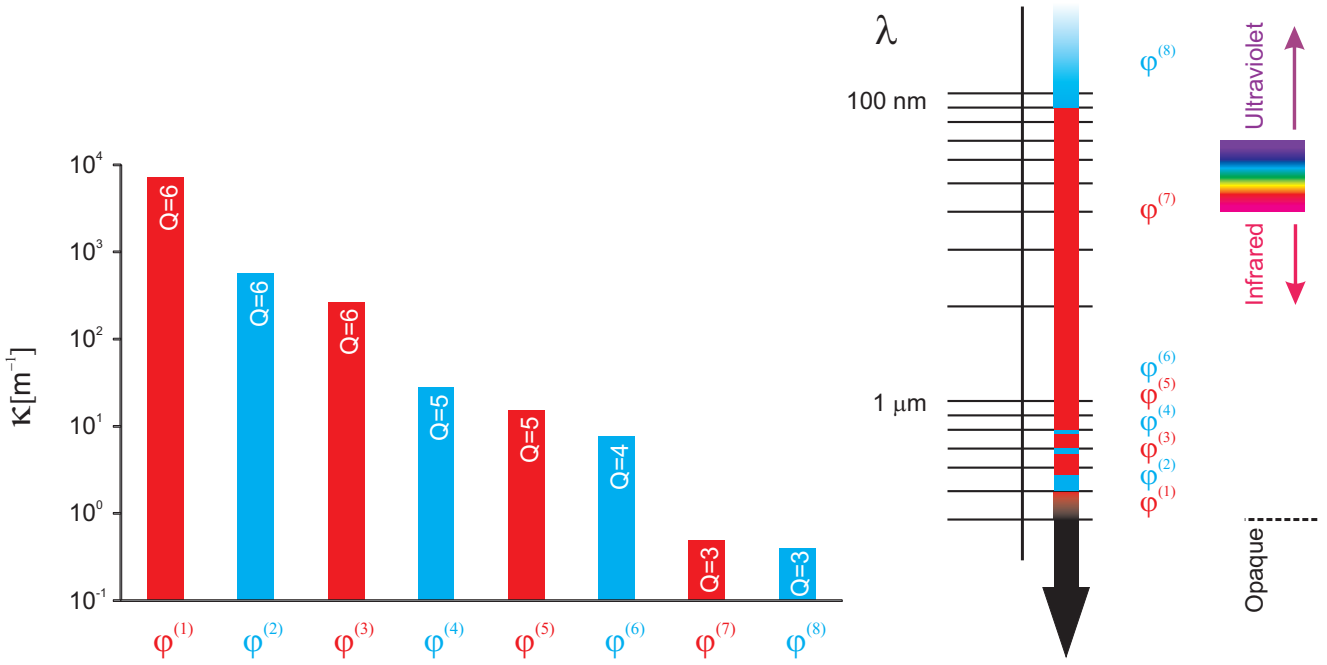

Figure 6.7: Eight-band model and the associated number of enrichments in the PUFEM for the test example of glass cooling in a disc enclosure.

example by retaining the same enrichment for the entire optical spectrum, *i.e.* the governing equations are solved without changing the enrichments for each frequency band. This is possible because the considered enrichment includes functions of a wide range of gradients from very steep to almost flat, which we have shown can be useful where no details are available on differences between radiation frequencies. Nevertheless, if these details are available then the PUFEM can be refined by defining an enrichment specific to each frequency band, such that functions with steep gradients are included in the enrichment only if the mean intensity $\varphi^{(k)}$ develops high gradients for the frequency band $[\nu_{k-1}, \nu_k)$. This refinement procedure can be significantly beneficial for radiative heat transfer models for which mean radiative intensities have to be computed for an optical spectrum with hundreds of frequency bands and only few of them require enrichment functions with steep gradients. In addition, note that one of the key advantages in using the linearly implicit time integration scheme in (3.1) with the PUFEM formulation is to allow for different enrichments to be used for each frequency band since a mean intensity $\varphi^{(k)}$ with $k = 1, 2, \ldots, 8$ can be solved independently of the other intensities. It is worth remarking that an h-refinement procedure in the FEM, to be equivalent to the q-refinement in the PUFEM, would require a different mesh to be assigned to each frequency band. This may be beneficial by reducing the computational costs of the solutions in some frequency bands. However, the interpolation needed to feed the radiation solution at all these bands back into the energy is enough to eliminate such benefit.

Based on a parametric study, not reported here for brevity in the presentation, it was observed that the mean radiative intensities $\varphi^{(7)}$ and $\varphi^{(8)}$ lead to a solution of a relatively uniform gradient over the computational domain. For the mean radiative intensities $\varphi^{(1)}$, $\varphi^{(2)}$ and $\varphi^{(3)}$, a sharp jump in the solution gradients is detected immediately on the domain boundary. As the domain releases its heat energy over time, this jump starts to dissipate, leading to a uniform gradient at late simulation times. This later phase is similar in term of its gradient to the solutions obtained for the mean radiative intensities $\varphi^{(7)}$ and $\varphi^{(8)}$. In the other frequency bands, namely for the intensities $\varphi^{(4)}$, $\varphi^{(5)}$ and $\varphi^{(6)}$, the obtained results illustrate transient behavior in resolving moderate solution gradients between the above two forms. Regarding the energy equation, the solution obtained for the temperature field exhibits similar behavior on the boundary as the solution obtained for the intensity $\varphi^{(1)}$ but with even sharper gradients at the early stage of the simulation. As the glass temperature approaches the ambient temperature, the heat released through

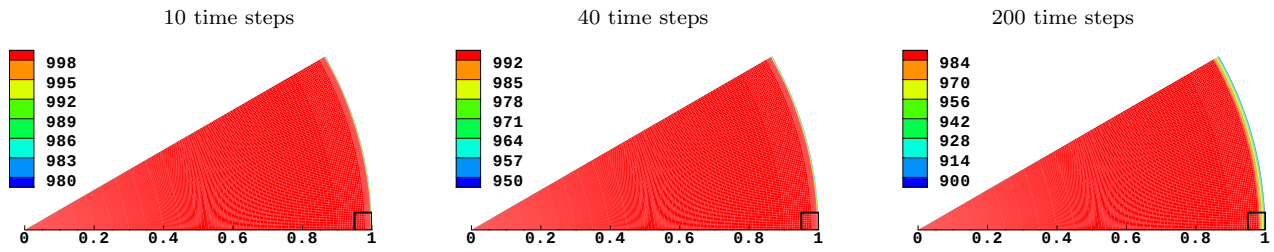

Figure 6.8: Temperature patterns obtained using the PUFEM at one element after 10 time steps (first column), 40 time steps (second column) and 200 time steps (third column). The square at the lower corner of the element is an indication of the zoom shown in Figure 6.9.

radiation and conduction ceases and steady-state solutions are obtained. To summarize, the energy equation starts at a steeper gradient compared to the solution of all mean radiative intensities. Furthermore, the intensities $\varphi^{(4)}$, $\varphi^{(5)}$, ..., $\varphi^{(8)}$ do not present steep gradients as in the first three bands. Therefore, the enrichment needed for the former bands is only a subset of the latter band enrichments which is in turn a subset of that of the energy equation.

Next we present the numerical simulations using the PUFEM with q-refinement. The number of hyperbolic functions used to enrich the PUFEM solution space for solving the energy equation is $Q = 7$. To solve the radiation equations for the mean intensities $\varphi^{(k)}$, with $k = 1, 2, \ldots, 8$, the number of enrichment functions is $Q = 6$ for $\varphi^{(1)}$, $\varphi^{(2)}$ and $\varphi^{(3)}$, whereas $Q = 5$ for $\varphi^{(4)}$ and $\varphi^{(5)}$. This number is reduced to $Q = 4$ for $\varphi^{(6)}$ and $Q = 3$ for $\varphi^{(7)}$ and $\varphi^{(8)}$. In Figure 6.7 we summarize the distribution of the number of enrichment functions within the considered spectrum of eight frequency bands. As can be seen from this figure, a large number of enrichment functions is required for large values of absorption coefficients. This is expected as the diffusion coefficients in the simplified P_1 equations (2.12) are inversely proportional to the absorption coefficients (*i.e.* $\varepsilon^2/3\kappa_k$) and steeper boundary layers are expected for smaller diffusion coefficients. Note that due to the global nature of the enrichment, the saving in the computational cost is proportional to the saving in the number of enrichments since the total number of degrees of freedom equals the number of nodes multiplied by the number of enrichments. For instance, the total number of degrees of freedom is reduced by half when solving for $\varphi^{(7)}$ compared to $\varphi^{(1)}$ in our simulations. Thus, almost one third of the computational cost in solving the radiation equation is saved when this refinement strategy is used compared to using a fixed number of enrichments $Q = 7$ for all $\varphi^{(k)}$, with $k = 1, 2, \ldots, 8$.

In Figure 6.8 we present snapshots of the temperature as recovered by the PUFEM on one element after 10, 40 and 200 time steps. In these simulations, the diffusion scale is $\varepsilon = 0.5$ and the timestep size is $\Delta t = 10^{-7}$. It can be seen that, at early simulation times, the domain temperature remains uniform except at the boundary layer. To have a better insight on the boundary layer a squared area appearing at the lower corner of the element in Figure 6.8 is zoomed. The zoomed region is shown in Figure 6.9 where the results obtained with FEMc and FEMf are plotted alongside the PUFEM results. It is clear that both the FEM and the PUFEM capture the same cooling features in the disc. However, by focusing on the zooming patterns it can be seen that the FEM on the coarse mesh exhibits non-physical oscillations at earlier time steps which are damped out as the simulation time progresses. These oscillations are reduced in the results obtained using FEMf but the PUFEM produces improved results for the time steps considered. The computed results for this test example suggest a more stable behavior with the PUFEM compared to FEMc and FEMf. Note that this accuracy in the PUFEM is achieved despite the fact that the total number of degrees of freedom for the PUFEM is only about 1% of that for FEMc.

In Figure 6.10 we illustrate the comparison, over a radial cross-section close to the domain boundary, of the temperature obtained using FEMc, FEMf and the PUFEM at six different instants. The oscillations at the earlier simulation times after 10 and 40 time steps can clearly be seen on the FEMc results near the disc boundary. These oscillations, due to the failure of FEMc to resolve boundary layers at earlier simulation times, are damped out as the cooling time increases. For all simulation times, the PUFEM resolves the

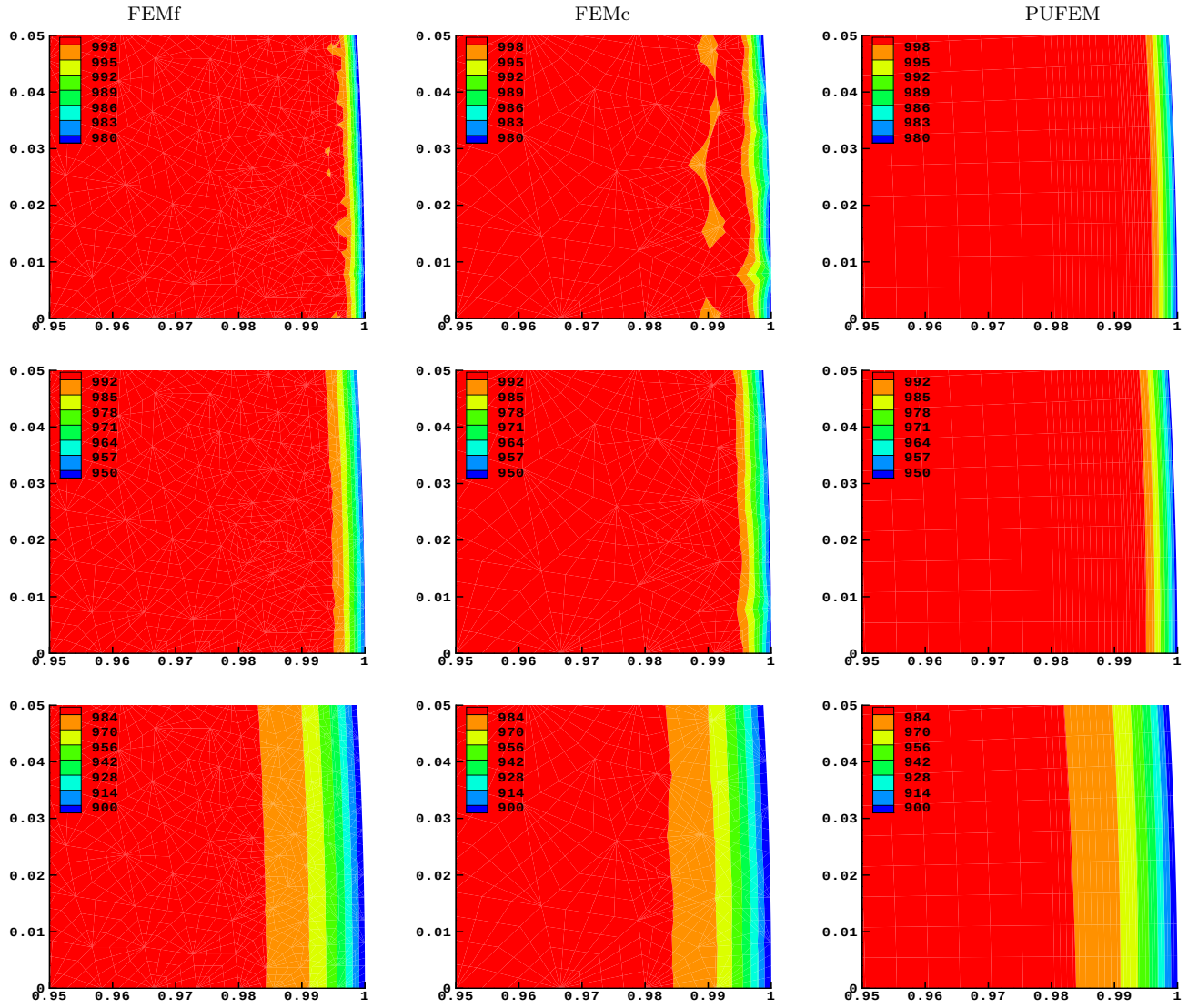

Figure 6.9: Temperature obtained using FEMf (first column), FEMc (second column) and the PUFEM (third column) after 10 time steps (first row), 40 time steps (second row) and 200 time steps (third row).

boundary layers without strong oscillations or excessive numerical dissipation and the temperature solutions closely match the FEMf results. At later simulation times FEMc, FEMf and the PUFEM results coincide well. To further examine the performance of the PUFEM we present in Figure 6.11 the radial cross-sections for the mean radiative intensities for six selected frequency bands after 10, 200 and 2000 time steps. The results obtained for $\varphi^{(5)}$ and $\varphi^{(8)}$ are not included in Figure 6.11 because they exhibit similar behavior to $\varphi^{(4)}$ and $\varphi^{(7)}$, respectively, but with different amplitudes. It is evident that the mean radiative intensities $\varphi^{(2)}$ and $\varphi^{(3)}$ develop steeper gradients than those associated with other frequency bands. Again spurious oscillations with different amplitudes are more pronounced in the FEMc results for the first three frequency bands after 10 and 200 time steps than in the PUFEM results. It should also be pointed out that the largest mean radiative intensity is calculated for the frequency band $\varphi^{(7)}$, compare the values of $\varphi^{(7)}$ in Figure 6.11. These computed solutions for the mean radiative intensity $\varphi^{(7)}$ dominate the other solutions in the remaining frequency bands. As a consequence, the smooth boundary layers in $\varphi^{(7)}$ may introduce stabilizing effects in the considered radiative heat transfer problem. As mentioned earlier, the pattern described above when refining the enrichment can be seen in Figure 6.10 and Figure 6.11 in the steeper gradient associated with the temperature as well as the mean radiative intensities $\varphi^{(1)}$, $\varphi^{(2)}$ and $\varphi^{(3)}$. A relatively flat gradient

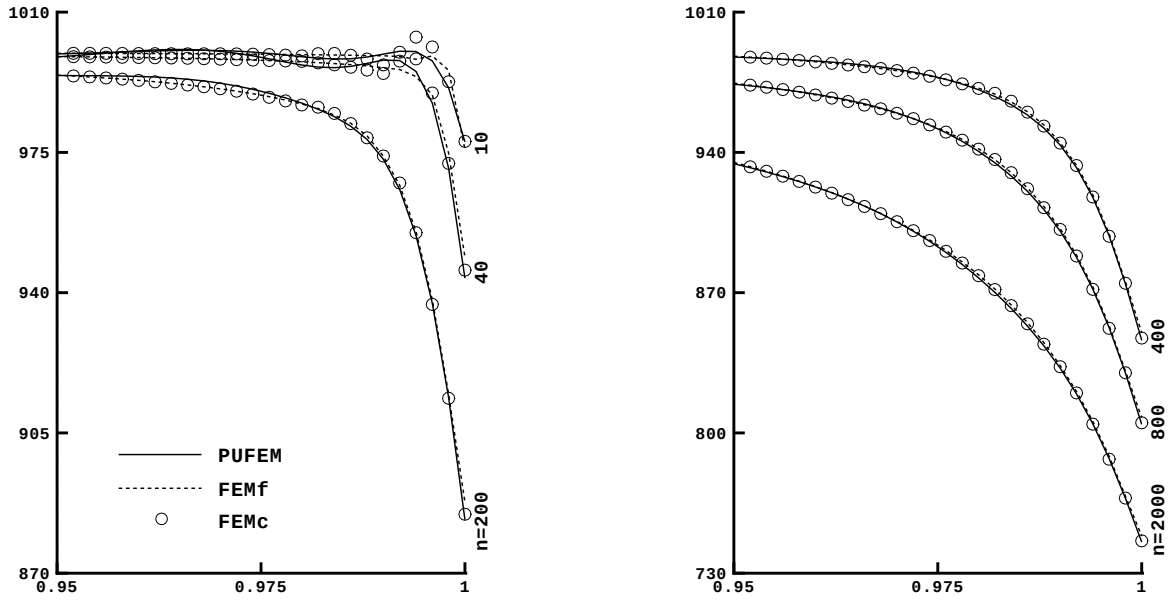

Figure 6.10: Comparison of radial cross-sections of the temperature obtained using FEMc, FEMf and the PUFEM at six different instants after $n = 10$, 40, 200, 400, 800 and 2000 time steps.

can be seen in the intensity $\varphi^{(7)}$. The PUFEM performs very satisfactorily for this frequency-dependent coupled problem since it does not diffuse the moving fronts and no spurious oscillations have been detected near steep gradients of the temperature field and radiative mean intensities in the computational domain.

7 Conclusions

A finite element method with adaptive enrichments for radiative boundary layers in glass cooling is presented. The governing equations consist of a semi-linear transient heat equation for the temperature field and a stationary simplified P_1 approximation for the radiative transfer in non-grey semitransparent media. It has been shown that the solution of radiative heat transfer at early time steps is a challenging task even when very fine meshes are used in the conventional FEM. Requiring only a small fraction of the number of degrees of freedom needed in the FEM, the proposed PUFEM shows better stability compared to that observed in the FEM. Indeed, because the main challenge in most glass cooling applications is related to the steep gradients at the boundary layers, it is found that embedding steep gradient enrichments circumvent any need to mesh refinement. Other than these steep gradients the solution can be very trivial and can be recovered with a very coarse finite element mesh. The advantages of the PUFEM with refined enrichments exploit this reduction in the number of degrees of freedom further for problems with large numbers of frequency bands, such as those found in industrially relevant simulations. The linearly implicit time-stepping scheme enables introducing a q-refinement procedure that is based on the boundary layer steepness at the first few time steps. The procedure defines a different number of enrichment functions to each frequency band when solving the radiation equation and it leads to a further reduction of more than 30% on top of the reduction already achieved by the hyperbolic enrichment procedure.

The performance of the proposed PUFEM method is analyzed for glass cooling of two enclosures in frequency-dependent media. For both test cases, it has been found that the FEM on fine meshes and the PUFEM exhibit similar results with the advantage of the PUFEM being more stable and leading to

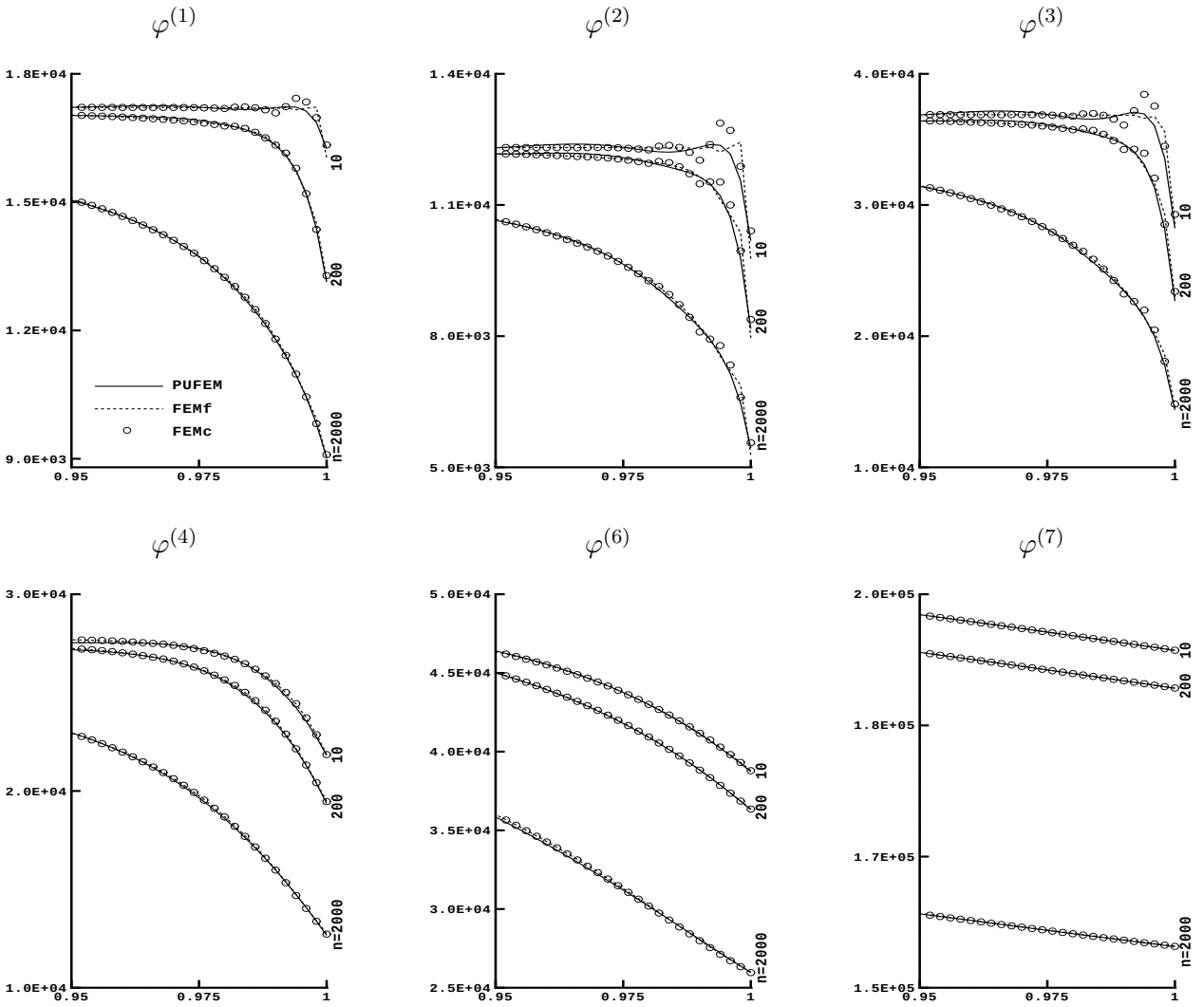

Figure 6.11: Comparison of radial cross-sections of the radiative mean intensities obtained using FEMc, FEMf and the PUFEM at three different instants after 10, 200 and 2000 time steps.

a drastic reduction in the computational costs compared to the FEM. The PUFEM and the FEM show differences at early simulation times which are more pronounced on the domain edges. It has also been found that the simplified P_1 approximation provides a simple way of incorporating the effects of thermal radiation, while keeping reasonable accuracy, and can be used in the cooling models of other materials as well. The tools presented in this paper illustrate how modelling techniques may be applied to support radiative heat transfer simulations. This indicates that the modeller can take advantage of the simplicity and low computational requirements of the PUFEM for the simplified P_1 model and use it with relative ease and confidence for describing the radiative heat transfer in glass cooling systems. Further work is necessary, however, to validate the models developed with experimental data in glass cooling. It should also be pointed out that the q-refinement procedure presented in this study can easily be extended to radiative heat transfer in different semitransparent materials when the relevant radiation spectrum is considered. However, this may also require the application of the enrichment functions to arbitrarily shaped geometries. One way to deal with geometrical irregularity in these materials is to apply the enrichment locally on the edges of the finite elements forming the boundaries of the computational domain. Results on this class of local enrichments will be reported in the near future.

References

[1] P. Bettess and J. Bettess. A profile matrix solver with built-in constraint facility. *Engineering Computations*, 3(3):209–216, 1986.

[2] W. Fiveland. The selection of discrete ordinate quadrature sets for anisotropic scattering. *ASME HTD. Fundam. Radiat. Heat Transfer.*, 160:89–96, 1991.

[3] M. Frank, M. Seaid, J. Janicka, A. Klar, R. Pinnau, and G. Thömmes. A comparison of approximate models for radiation in gas turbines. *Int. J. Progress in CFD*, 3:191–197, 2004.

[4] E.M. Gelbard. *Simplified Spherical Harmonics Equations and their Use in Shielding Problems.* Technical Report WAPD-T-1182, Bettis Atomic Power Laboratory, 1961.

[5] T. Götz. Coupling heat conduction and radiative transfer. *J. Quant. Spectr. Radiative Transfer.*, 72:57–73, 2002.

[6] ITWM. *Fraunhofer-Institut für Techno- und Wirtschaftsmathematik, Kaiserslautern, Germany.* http://www.itwm.de.

[7] A.J. Juhasz. An analysis and procedure for determining space environmental sink temperatures with selected computational results. In *Energy Conversion Engineering Conference and Exhibit, 2000. (IECEC) 35th Intersociety*, pages 1175 – 1183. American Institute of Aeronautics and Astronautics, 2000.

[8] A. Klar, J. Lang, and M. Seaid. Adaptive solutions of SP_N-approximations to radiative heat transfer in glass. *Int. J. Therm. Sci.*, 44:1013–1023, 2005.

[9] E. Larsen, J. Morel, and J. McGhee. Asymptotic derivation of the multigroup P_1 and simplified P_N equations with anisotropic scattering. *Nucl. Sci. Eng.*, 123:328–367, 1996.

[10] E. Larsen, G. Thömmes, A. Klar, M. Seaid, and T. Götz. Simplified P_N approximations to the equations of radiative heat transfer and applications. *J. Comp. Phys.*, 183:652–675, 2002.

[11] G. Lauriat. Combined radiation-convection in gray fluids enclosed in vertical cavities. *J. Heat Transfer.*, 104:609–615, 1982.

[12] E. Lewis and W. Miller. *Computational Methods of Neutron Transport.* John Wiley & Sons, New York, 1984.

[13] F. Liu, H. Becker, and Y. Bindar. A comparative study of radiative heat transfer modelling in gas-fired furnaces using the simple grey gas and the weighted-sum-of grey-gases models. *Int. J. Heat Mass Tran.*, 41:3357–3371, 1998.

[14] J.M. Melenk and I. Babuška. The partition of unity finite element method: Basic theory and applications. *Comput. Methods Appl. Mech. Engrg*, 139:289–314, 1996.

[15] D. Mihalas and B.S. Mihalas. *Foundations of Radiation Hydrodynamics.* Oxford University Press, New York, 1983.

[16] M.F. Modest. *Radiative Heat Transfer.* McGraw-Hill, 1993.

[17] M.S. Mohamed, M. Seaid, J. Trevelyan, and O. Laghrouche. A partition of unity fem for time-dependent diffusion problems using multiple enrichment functions. *Int. J. Numer. Meth. Engng.*, 93:245–265, 2013.

[18] M.S. Mohamed, M. Seaid, J. Trevelyan, and O. Laghrouche. Time-independent hybrid enrichment for finite element solution of transient conduction-radiation in diffusive grey media. *J. Comp. Phys.*, 251:81–101, 2013.

[19] E.A. Munts, S.J. Hulsho, and R. de Borst. The partition-of-unity method for linear diffusion and convection problems: accuracy, stabilization and multiscale interpretation. *Int. J. Numer. Meth. Engng.*, 43:199–213, 2003.

[20] P. O'Hara, C.A. Duarte, and T. Eason. Transient analysis of sharp thermal gradients using coarse finite element meshes. *Comput. Methods Appl. Mech. Engrg.*, 200:812–829, 2011.

[21] G.C. Pomraning. *The Equations of Radiation Hydrodynamics*. Pregamon press, 1973.

[22] S. Rosseland. *Theoretical Astrophysics: Atomic Theory and the Analysis of Stellar Atmospheres and Envelopes*. Clarendon Press, Oxford, 1936.

[23] M. Seaid. Multigrid newton-krylov method for radiation in diffusive semitransparent media. *J. Comp. Applied Math.*, 203:498–515, 2007.

[24] M. Seaid, M Frank, A. Klar, R. Pinnau, and G. Thömmes. Efficient numerical methods for radiation in gas turbines. *J. Comp. Applied Math.*, 170:217–239, 2004.

[25] M. Seaid and A. Klar. Efficient preconditioning of linear systems arising from the discretization of radiative transfer equation. *Lect. Notes. Comp. Sci.*, 35:211–236, 2003.

[26] I. Teleaga, M. Seaid, I. Gasser, A. Klar, and J. Struckmeier. Radiation models for thermal flows at low mach number. *J. Comp. Phys.*, 215:506–525, 2006.

[27] G. Thömmes, R. Pinnau, M. Seaid, T. Götz, and A. Klar. Numerical methods and optimal control for glass cooling processes. *Transp. Theory Stat. Phys.*, 31:513–529, 2002.

[28] F.P. van der Meer, R. Al-Khoury, and L.J. Sluys. Time-dependent shape functions for modeling highly transient geothermal systems. *Int. J. Numer. Meth. Engng.*, 77:240–260, 2009.